Geophysical Journal International

Geophys. J. Int. (2013) **194,** 100–117
Advance Access publication 2013 April 22

doi: 10.1093/gji/ggt113

The tectonic crustal stress field and style of faulting along the Pacific North America Plate boundary in Southern California

Wenzheng Yang* and Egill Hauksson

Seismological Laboratory, Division of Geological and Planetary Sciences, California Institute of Technology, CA 91125, *USA.*
E-mail: wenzheng@gps.caltech.edu

Accepted 2013 March 19. Received 2013 March 12; in original form 2012 October 22

SUMMARY

We invert for the state of stress in the southern California crust using a catalogue of high quality earthquake focal mechanisms (1981–2010). The stress field is best resolved where seismicity rates are high and sufficient data are available to constrain the stress field across most of the region. From the stress field, we determine the maximum horizontal compressive stress (S_{Hmax}) orientations and the style of faulting across southern California. The trend of S_{Hmax} exhibits significant regional and local spatial heterogeneities. The regional trend of S_{Hmax} varies from north along the San Andreas system to NNE to the east in the Eastern California Shear Zone as well as to the west, within the Continental Borderland and the Western Transverse Ranges. The transition zones from one state of stress to the other occur over a distance of only a few kilometres, following a trend from Yucca Valley to Imperial Valley to the east, and the western edge of the Peninsular Ranges to the west. The local scale heterogeneities in the S_{Hmax} trend include NNW trends along the San Andreas Fault near Cajon Pass, Tejon Pass and the Cucapah Range, as well as NNE trends near the northern San Jacinto Fault and the Wheeler Ridge area. The style of faulting exhibits similar complexity, ranging from predominantly normal faulting in the high Sierra Nevada, to strike-slip faulting along the San Andreas system, to three consecutive bands of thrust faulting in the Wheeler Ridge area and the Western Transverse Ranges. The local variations in the style of faulting include normal faulting at the north end of the San Jacinto Fault and scattered areas of thrust faulting. The regional variations in the S_{Hmax} trends are very similar to the pattern of the GPS-measured maximum shortening axes of the surface strain rate tensor field although the strain field tends to be smoother and appears to capture some of the upper-mantle deformation field. The mean trend of S_{Hmax} departs about approximately 14° to the east from the trend of the maximum shortening directions derived from anisotropy in the upper mantle.

Key words: Seismicity and tectonics; Continental margins: transform; Dynamics: seismotectonics; High strain deformation zones; Crustal structure; North America.

1 INTRODUCTION

The geometrically complex tectonic boundary between the Pacific and the North America plates cuts across southern California causing a broad distribution of seismicity (Fig. 1). The right-lateral San Andreas Fault (SAF), together with subparallel and conjugated strike-slip faults account for the majority of the seismicity, which exhibits strike-slip faulting. North–south compression in the west trending Transverse Ranges, produces reverse faulting earthquakes, which account for a small fraction of the total seismicity. Areas with high topography, such as the Sierra Nevada in the north, accommodate mostly small normal faulting earthquakes. To understand the contemporary seismotectonic processes along this boundary, we use the earthquake data to determine the crustal stress field. We interpret the stress field in the context of both local and regional tectonics.

The crustal stress field can also be estimated from geological observations such as slickenside data collected on fault surfaces. At shallow depth (≤3.5 km), well borehole breakouts or orientations of hydraulic fractures stress measurements have been applied to infer the orientation of maximum horizontal stress (e.g. Zoback *et al.* 1985; Zoback & Healy 1992). For stress state in the crust (from 0 to 20 km depth), several inversion methods have been proposed to calculate the orientation of stress field and relative strength among principle stresses from earthquake focal mechanisms (e.g. Ellsworth & Zhonghuai 1980; Angelier 1984; Gephart & Forsyth

* Now at: Air Worldwide, 131 Dartmouth Street, Boston, MA 02116, USA.

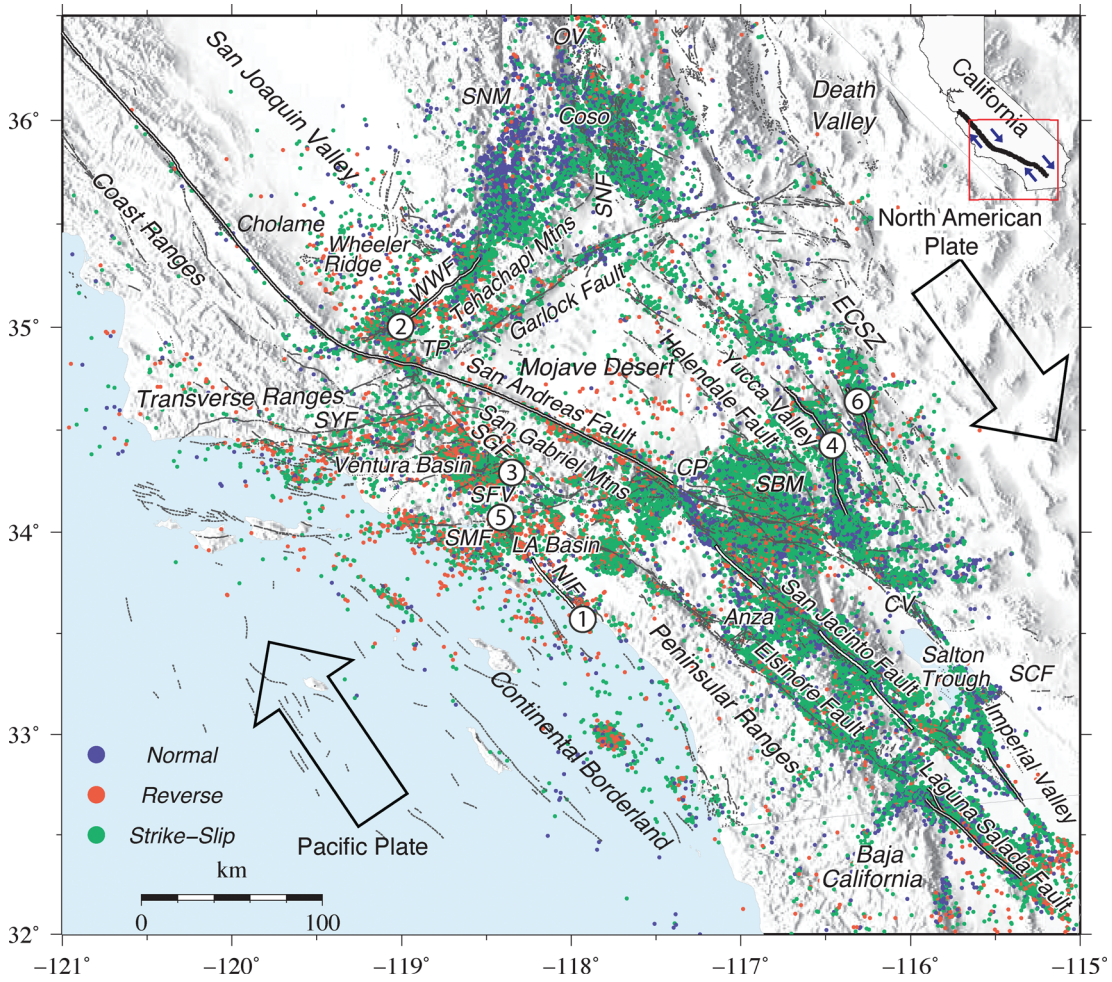

Figure 1. 179 000 locations of earthquake focal mechanisms coloured according to sense of motion in southern California. Fault traces mapped by Jennings (1994) are in grey. Surface ruptures since the 1857 Fort Tejon earthquake of major strike-slip main shocks are in white. The inset panel on the top right-hand corner shows the relative location of the mapped area in the whole state of California, with the San Andreas Fault in bold, and relative plate motions with arrows. CP, Cajon Pass; CV, Coachella Valley; ECSZ, Eastern California Shear Zone; NIF, Newport-Inglewood Fault; OV, Owens Valley; SBM, San Bernardino Mountains; SFV, San Fernando Valley; SGF, San Gabriel Fault; SMF, Santa Monica Fault; SNF, Sierra Nevada Fault; SNM, Sierra Nevada Mountains; SYF, Santa Ynez Fault; TP, Tejon Pass; WWF, White Wolf Fault. Circles with labels from 1 to 6 mark the epicentres of the 1933 Long Beach M_w 6.4 earthquake, the 1952 Kern county M_w 7.3 earthquake, the 1971 San Fernando M_w 6.6 earthquakes, the 1994 Northridge M_w 6.7, the 1992 M_w 7.4 Landers earthquake and the 1999 M_w 7.1 Hector Mine earthquake, respectively.

1984; Michael 1984; Hardebeck & Michael 2006) with the assumption that faults slip in the direction of shear stress (Wallace 1951; Bott 1959). Among all types of measurements, stress orientations inferred from earthquake focal mechanisms constitute the bulk (72 per cent) of the world stress map (WSM) database (Heidbach *et al.* 2010), and thereby serve as the major contributor to stress field analysis.

Previously, using focal mechanisms from ∼50 000 earthquakes recorded by the Southern California Seismic Network (SCSN) from 1981 to 1999, Hardebeck & Hauksson (2001b) inverted for the state of stress in southern California. Their results showed that the SAF in southern California is a weak fault in a low-strength crust. With additional 10 more years of high quality data in the YHS2010 catalogue (Yang *et al.* 2012), we obtain images of the stress field in southern California with improved coverage and much higher resolution than was available before.

In this study, using the YHS2010 catalogue to invert for the state of stress, we determine the orientation of the maximum horizontal compressive stress (S_{Hmax}) and the style of faulting across the region. We analyse regional and local patterns of stress orientations and faulting styles in context of the local tectonics. Furthermore, we compare the orientations of S_{Hmax} with the available surface strain rate tensor field determined from Global Positioning System (GPS) velocities (Holt *et al.* 2010) and mantle anisotropy results determined from SKS shear wave splitting analysis for southern California region as available in the shear wave splitting database (Wüstefeld *et al.* 2009). Our results provide new insights into the regional and local tectonics along the plate boundary.

2 DATA AND METHOD

The YHS2010 catalogue includes approximately 179 000 high quality earthquake focal mechanisms for local earthquakes recorded by the SCSN from 1981 January 1 to 2010 December 31 with depth generally in 0–20 km. To ensure high quality, each event in the catalogue has at least eight *P*-wave polarities with an azimuthal gap of less than 175°. Each earthquake in this catalogue was fitted by a double-couple earthquake source with *P*-wave polarities

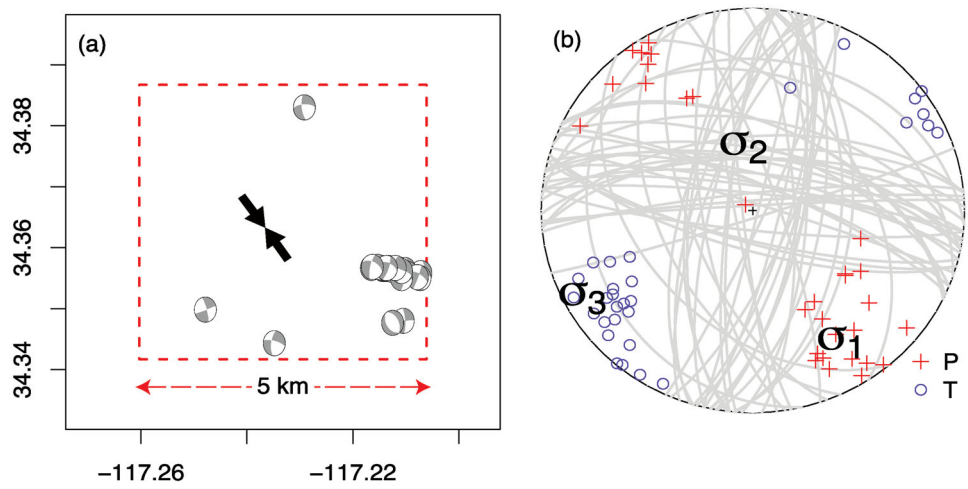

Figure 2. Illustration of one result given by SATSI to the scheme of grid size = 5 km and number of event = 30 per grid node. (a) Employed $N = 30$ focal mechanisms (grey beachballs) inside the grid (dashed red square), the black arrow marks the direction of calculated S_{Hmax}. (b) Nodal planes (grey curves), P-axis (red crosses) and T-axis (blue circles) for the $N = 30$ employed earthquakes. Orientations of the inverted three principal axes (σ_1, σ_2 and σ_3) are labelled.

and available S/P amplitude ratios using the HASH method (Hardebeck & Shearer 2002, 2003). For the stress inversion method, we use the Spatial And Temporal Stress Inversion (SATSI) program (Hardebeck & Michael 2006) available from the USGS webpage. Previously, Hardebeck & Hauksson (2001a) demonstrated that the stress inversion method by Michael (1984, 1987), which is used as the algorithm in the SATSI, is able to produce accurate results even for low quality data.

To obtain results with the highest possible spatial resolution and coverage, we perform stress inversions at different spatial scales. We perform four independent 2-D stress inversions at two grid scales (5 km, 10 km), and with two numbers of events per grid node ($N =$ 30, $N = 15$). To study possible variation of the stress field with depth, we perform a 3-D stress inversion with a 5-km scaled cubic grid and 30 events per grid node. Because the number of events per grid node is not evenly distributed in space, we use the following approaches to select data for each grid node. For grid nodes with abundant seismicity, we randomly select N events of the highest focal mechanism quality. For grid nodes where seismicity is sparse, we search the neighbouring area with twice the grid scale for events to match the N number. If not enough events were available, the grid node was excluded from the inversion. For the SATSI inversion, we use a damping value of 1.2, which was derived by analysing the trade-off between data misfit and model length, which is a measure of the degree of heterogeneity in the solution (Hardebeck & Michael 2006).

Hardebeck & Hauksson (2001b) showed that stress orientations are typically well resolved only with focal mechanism diversity (defined as the rms angular difference from the mean focal mechanism) of $>40^\circ$ when using focal mechanisms with nodal plane ambiguity of 10°–20°. The smallest grid scale used in this study is 5 km, which is the same grid scale as used in Hardebeck & Hauksson (2001b). Although we take $N = 15$ or 30 events per grid, which are smaller, the associated focal mechanism diversities are generally very similar. More importantly, we apply the inversion method of Hardebeck & Michael (2006), which performs stress inversion of a single grid node together with its immediate neighbouring nodes, instead of a limited data set that belongs to a single grid node. Consequently, the possible lack of focal mechanism diversity at a single grid node is significantly reduced.

The results of the inversions consist of the best-fitting orientations of the three principal stress axes in both the trends and plunge angles, and the stress ratio [$R = (\sigma_1 - \sigma_2)/(\sigma_1 - \sigma_3)$, where σ_1, σ_2 and σ_3 are the three principal stress magnitudes ordered from most compressional to most tensional (Angelier 1979)] at each grid node. The inversion also provides an uncertainty range (95 per cent confident level from 1000 bootstraps) for each best-fitting parameter. From the inverted directions of the three principal stresses and the stress ratio, we apply the algorithm proposed by Lund & Townend (2007) to calculate the direction of the maximum horizontal stress (S_{Hmax}). Similar to Hardebeck & Hauksson (2001b), we use the Anderson fault parameter, A_ϕ, as defined by Simpson (1997), to quantitatively compare tectonic regimes based on stress ratios and rake angles. $A_\phi = (n + 0.5) + (-1)^{\mathrm{n}} \times (R - 0.5)$, where $n =$ 0, 1 and 2 for normal, strike-slip and reverse types, respectively. Consequently, A_ϕ increases monotonically in range 0.0–1.0 for normal faulting, 1.0–2.0 for strike-slip faulting, and 2.0–3.0 for reverse faulting.

As an example, in Fig. 2 we show a data set of focal mechanisms, and the inversion results for one grid node (located in the San Bernardino Mountains) where we use a grid scale of 5 km and 30 events per grid node (hereafter refer as G05N30).

3 RESULTS

3.1 Stress field and resolution

The cumulative probabilities of the 95 per cent confidence intervals for the seven parameters determined with the four stress inversions are shown in Figs 3(a)–(g). For the trend error of the three principal axes, the 1σ (68 per cent) uncertainty is in the range of 11°, 32° and 10° for lower and upper 95 per cent confidence intervals of σ_1, σ_2 and σ_3, respectively. The cumulative probability decreases rapidly with the decrease of the angular difference from the best-fitting trend. The confidence intervals of the plunge values for σ_1, σ_2 and σ_3 are less well constrained because the axes with large plunge angles can be relatively scattered. The 1σ uncertainty is in the range of $[-47^\circ, 34^\circ]$, $[-60^\circ, 27^\circ]$ and $[-25^\circ, 17^\circ]$ for lower and upper 95 per cent confidence intervals of σ_1, σ_2 and σ_3, respectively. The

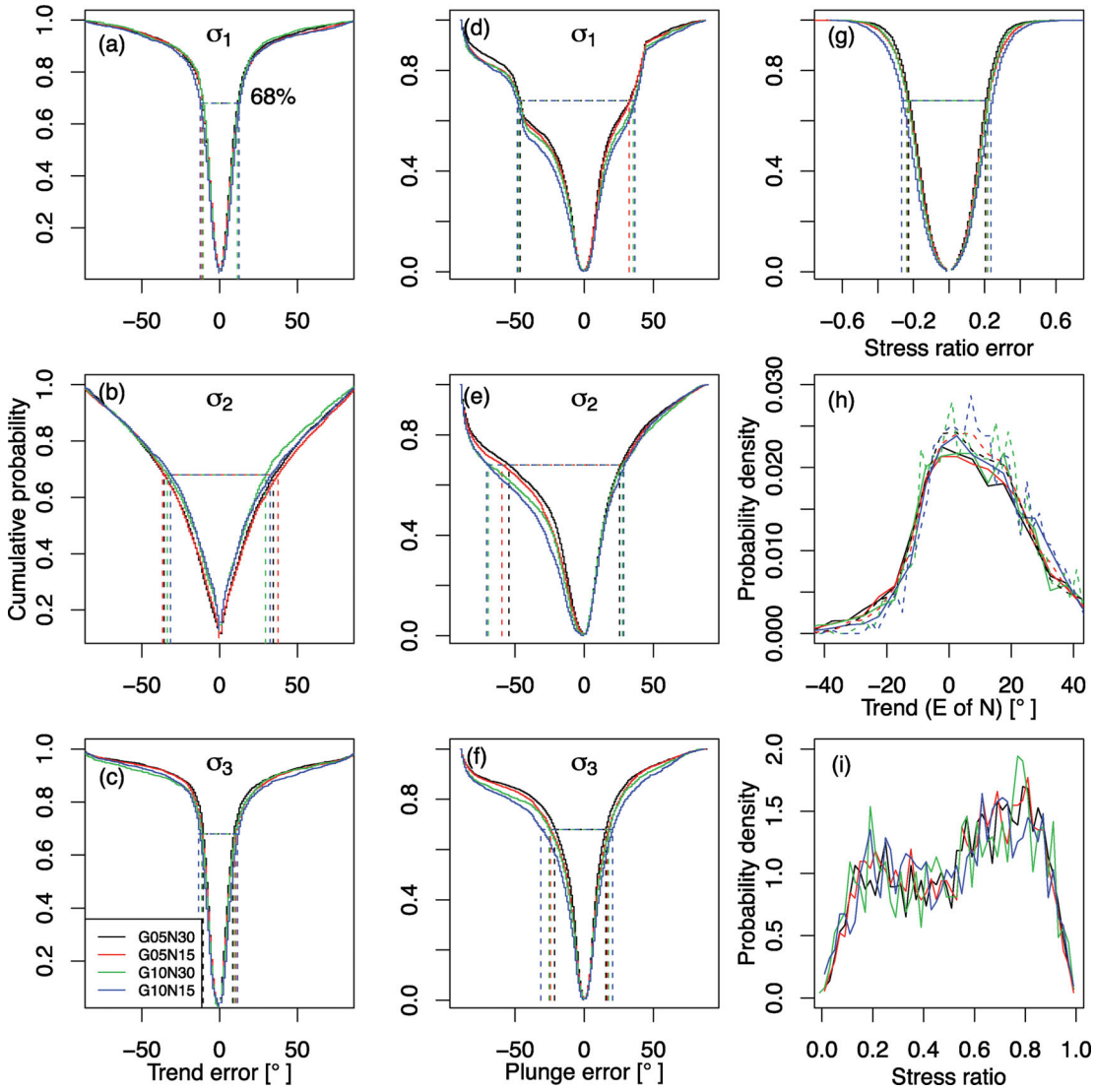

Figure 3. Distributions of the inverted parameters (solid curves) for the four schemes: G05N30 (grid scale in 5 km and 30 events per grid node), G05N15 (grid scale in 5 km and 15 events per grid node), G10N30 (grid scale in 10 km and 30 events per grid node), and G10N15 (grid scale in 10 km and 15 events per grid node). (a)–(c) Cumulative probability functions of the lower and upper 95 per cent confidence intervals for trends of σ_1, σ_2 and σ_3 (labelled in each panel). Horizontal dashed lines mark the 1σ uncertainty (68 per cent), and vertical dashed lines mark the associated low and upper errors. (d)–(f) Cumulative probability functions of the lower and upper 95 per cent confidence intervals for plunges of σ_1, σ_2 and σ_3 (labelled in each panel). (g) Cumulative probability functions of the low and upper 95 per cent confidence intervals for stress ratio. (h) Probability densities of trends of σ_1 and S_{Hmax} (dashed curves). (i) Probability densities of stress ratios. Legend of schemes in different colours is in the bottom left-hand corner in (c).

1σ uncertainty for stress ratios is approximately 0.24 (Fig. 3g). The distribution of best-fitting σ_1-trends matches with the distribution of S_{Hmax} trends, and is stable over different inversion schemes (Fig. 3h). The distributions of the stress ratios are also similar for different inversions.

The inversions resolve the maximum principal stress orientations to an uncertainty of 11° or less although in some cases the 95 per cent confidence interval may extend to 30° due to normal faulting stress regime. The spatial resolution of the 95 per cent confidence interval (P_{95}) in the azimuth of σ_1 for each of the four schemes is fairly uniform across the whole region except for the southern Sierra Nevada and a few scattered areas, which have limited seismicity (Fig. 4). Similarly, the spatial resolution of the P_{95} in the stress ratios for each of the four inversions is fairly uniform across the region (Fig. 5). Areas with relatively large stress ratio uncertainties include the Lander-Hector Mine area and other places that are distributed almost randomly and close to the edge of data coverage. For both parameters, the spatial resolution decreases as the grid size increases or fewer events per grid node are available.

The spatial distribution of the S_{Hmax} trend and A_ϕ from the 2-D SATSI inversions show the trade-off between spatial resolution and coverage (Figs 6 and 7). The spatial distributions of S_{Hmax} trends and A_ϕ values are similar for the different choices of grid size or number of events per grid. Similar to Hardebeck & Hauksson (2001b), the most likely S_{Hmax} trend is in N7°E (Fig. 3h). With additional data accumulated during the last 10 yr, a higher resolution of the stress field is available in more areas with low seismicity rates, and improved coverage extends to areas where earthquakes occurred over the recent decade, such as in the 2010 El Mayor Cucapah M_{w} 7.2 main shock aftershock zone across the U.S.–Mexico international border.

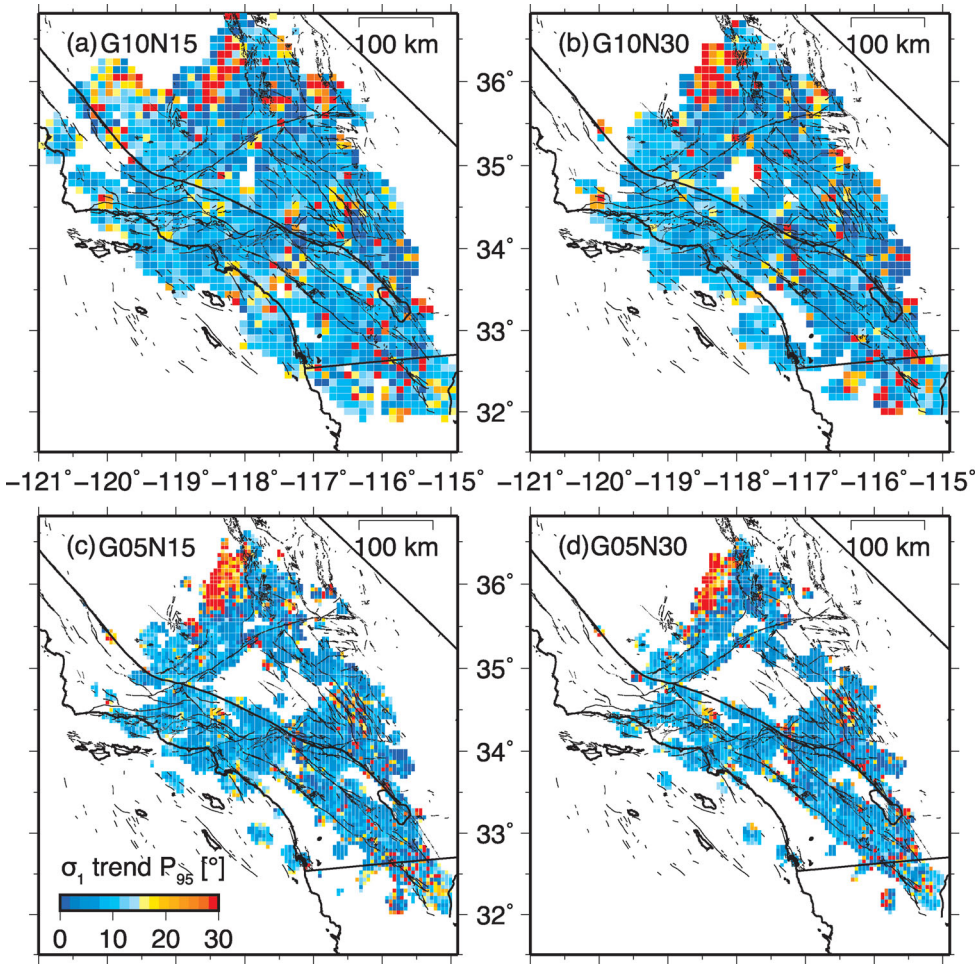

Figure 4. Spatial distribution of the 95 per cent confidence interval (P_{95}) of the σ_1 trends for (a) grid scale of 10 km and 15 events per grid node (G10N15); (b) grid scale of 10 km and 30 events per grid node (G10N30); (c) grid scale of 5 km and 15 events per grid node (G05N15); (d) grid scale of 5 km and 30 events per grid node (G05N30). The colour legend is at the bottom left-hand side in (c).

We concentrate the analysis on the 2-D spatial inversion because the results of the inversions do not vary significantly with time or depth. From the images of S_{Hmax} trends, our results provide improved resolution of the stress field in the East California Shear Zone (ECSZ) and the San Fernando Valley that have clear S_{Hmax} orientations in NNE. When compared to Hardebeck & Hauksson (2001b) and Hartse *et al.* (1994), our results provide improved resolution of an anomalous area with S_{Hmax} orientations in NNE elongates along the San Jacinto Fault (SJF) to the west of Anza. Furthermore, our results provide more detailed information about the boundaries of regions with S_{Hmax} orientations in NNE both on regional and local scales. The NNE S_{Hmax} orientation zone in the east of southern California is not only limited in the ECSZ as documented in Hardebeck & Hauksson (2001b). Instead, this zone extends further southward to the Imperial Valley. Similarly, the NNE S_{Hmax} orientation zone west of the SAF extends along the Newport-Inglewood Fault (NIF) into the Continental Borderland, forming a broad north–northwest trending zone in the S_{Hmax} images of 10-km grid scale (Figs 6a and b). On a local scale, besides the northern part of the SJF near Anza, additional areas with NNE S_{Hmax} exist in the Transverse Ranges, the San Joaquin Valley, and along the Sierra Nevada Fault (SNF; Fig. 6a). In the image of 5-km grid scale (Figs 6c and d), these local NNE S_{Hmax} heterogeneities generally extend along or are confined by traces of major faults.

The style of faulting (A_ϕ) is dominated by strike-slip faulting along the SAF system (Fig. 7). To the west, the Transverse Ranges are dominated by thrust faulting, and the southern Sierra Nevada Mountains are dominated by normal faulting. A small N–S region with normal faulting much more clearly defined as compared to previous studies, exists adjacent to the SAF in the Cajon Pass, where the SJF obliquely joins with the SAF. Previously, a less clear image was available (Jones 1988; Hardebeck & Hauksson 2001b).

Each of the four inversions has advantages and disadvantages. Results of G10N15 (Figs 6a and 7a) provide the best spatial coverage, but have low spatial resolution in areas of both high and low seismicity. Comparatively, results of G05N30 (Figs 6d and 7d) provide the finest resolution in areas with high seismicity, which can be used to study stress field variation on a local scale, but do not provide information for areas with sparse seismicity. Therefore, it is worthwhile to synthesize results from multiple scales and interpret the stress fields with reference to each other. Here, we overlap images from results with the highest resolution (G05N30) and results with the best spatial coverage (G10N15) for composite images, and synthesize several representative profiles in southern California with 0.2° in width, and stack results from all resolutions along each profile for S_{Hmax} (Figs 8 and 9), and style of faulting (Figs 10 and 11), respectively. The GPS provides precise measurement of relative plate motions at the surface of the

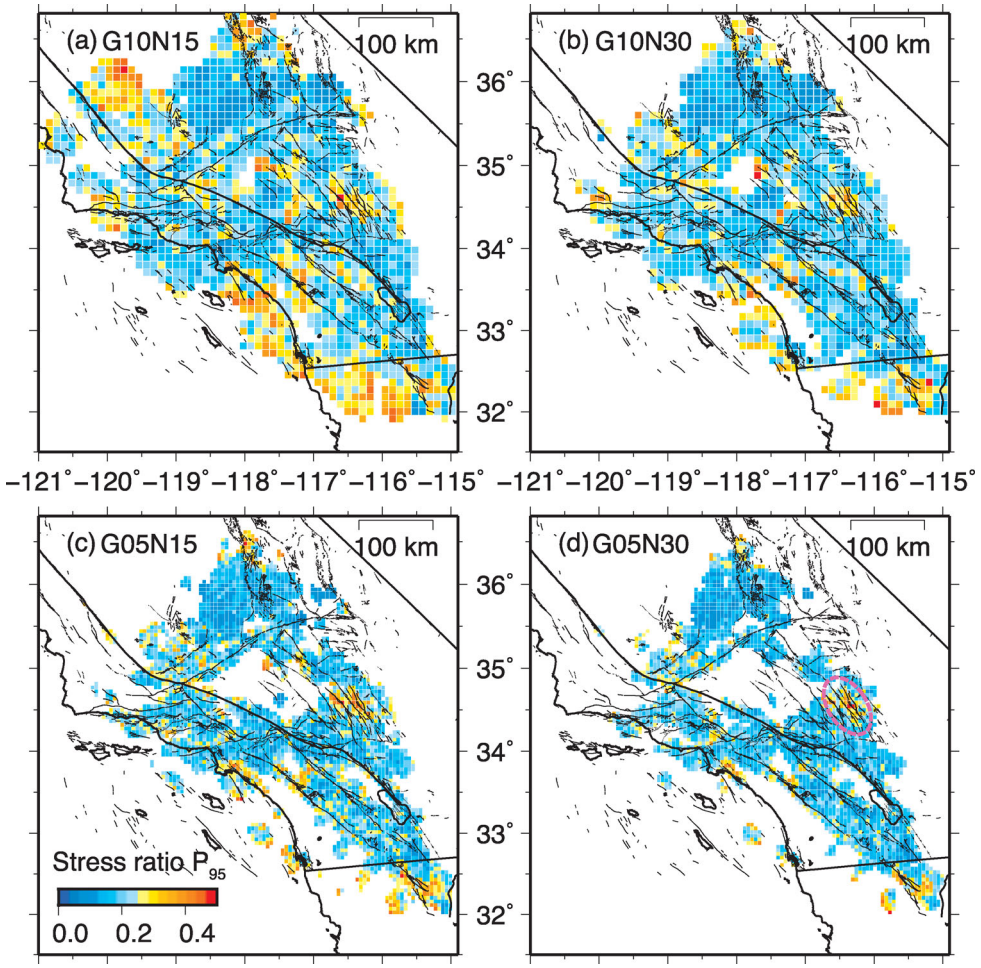

Figure 5. Spatial distribution of the 95 per cent confidence interval (P_{95}) in the stress ratio for (a) grid scale of 10 km and 15 events per grid node (G10N15); (b) grid scale of 10 km and 30 events per grid node (G10N30); (c) grid scale of 5 km and 15 events per grid node (G05N15); (d) grid scale of 5 km and 30 events per grid node (G05N30). The colour legend is at the bottom left-hand side in (c). The pink ellipse in (d) marks the Landers–Hector Mine area.

Earth. In southern California, the long-term surface velocity field has been determined from GPS (e.g. Shen *et al.* 2011). Both the stress field inverted from earthquake focal mechanisms in the crust and the velocity field observed with GPS at the surface, reflect tectonic deformation. In Figs 9 and 11, we add the GPS velocities of stations (Shen *et al.* 2011) in the representative profiles to demonstrate that both measurements of crustal deformation behave similarly.

3.2 Heterogeneities in S_{Hmax}

Stress field in the lithosphere could be classified into global scale (first-order, >500 km) and regional scale (second-order, 100–500 km; Zoback 1992). Recent studies with denser data sets (e.g. Heidbach *et al.* 2010; Montone *et al.* 2012) suggested the existence of stress heterogeneity on local scale (third-order, <100 km). These local scale stress patterns are controlled by phenomena such as active faulting, gravitational collapse, local intrusions, density contrasts, or detachment faults. Because the local scale stress patterns are of similar spatial extent as the rupture zone of a major earthquake (M_w 7.0), they are important for understanding the mechanisms of faulting in earthquakes. We identify changes in the stress patterns, and discuss these patterns on both regional and local scales.

As shown here and in previous studies, the regional trend of S_{Hmax} in central to southern California is generally along the NNE direction (Mount & Suppe 1992; Zoback 1992; Townend & Zoback 2004), and the most likely S_{Hmax} trend in southern California is at N7°E (Hardebeck & Hauksson 2001b). The composite image of S_{Hmax} trends reveals several regional and local stress heterogeneities that vary in spatial scale and degree of heterogeneity (Fig. 8).

3.2.1 *Eastern California Shear Zone*

The Eastern California Shear Zone (ECSZ) extends to the east of the grey and solid dashed curves ('YIV-L' in Fig. 8), which are generally located to the east of the SAF inside the North America Plate. In general, the trend of S_{Hmax} in the ECSZ ranges from N20°E as the background level to N40°E in the Landers and Hector Mine rupture areas. Geodetically, the slip rate in the ECSZ together with the Walker Lane Belt (WLB) to the north (~12 mm yr^{-1}) accommodates approximately 20–25 per cent of the present-day relative plate motion along the Pacific-North American Plate boundary (Sauber *et al.* 1994; Thatcher *et al.* 1999). The S_{Hmax} orientation in the ECSZ is relatively homogeneous except for a small area with a NNW orientation of S_{Hmax} at the southeast corner of the Salton Trough (Fig. 8). Near the Landers rupture zone, the S_{Hmax} orientations are more scattered as resolution increases (profile HH′ in Fig. 9), which

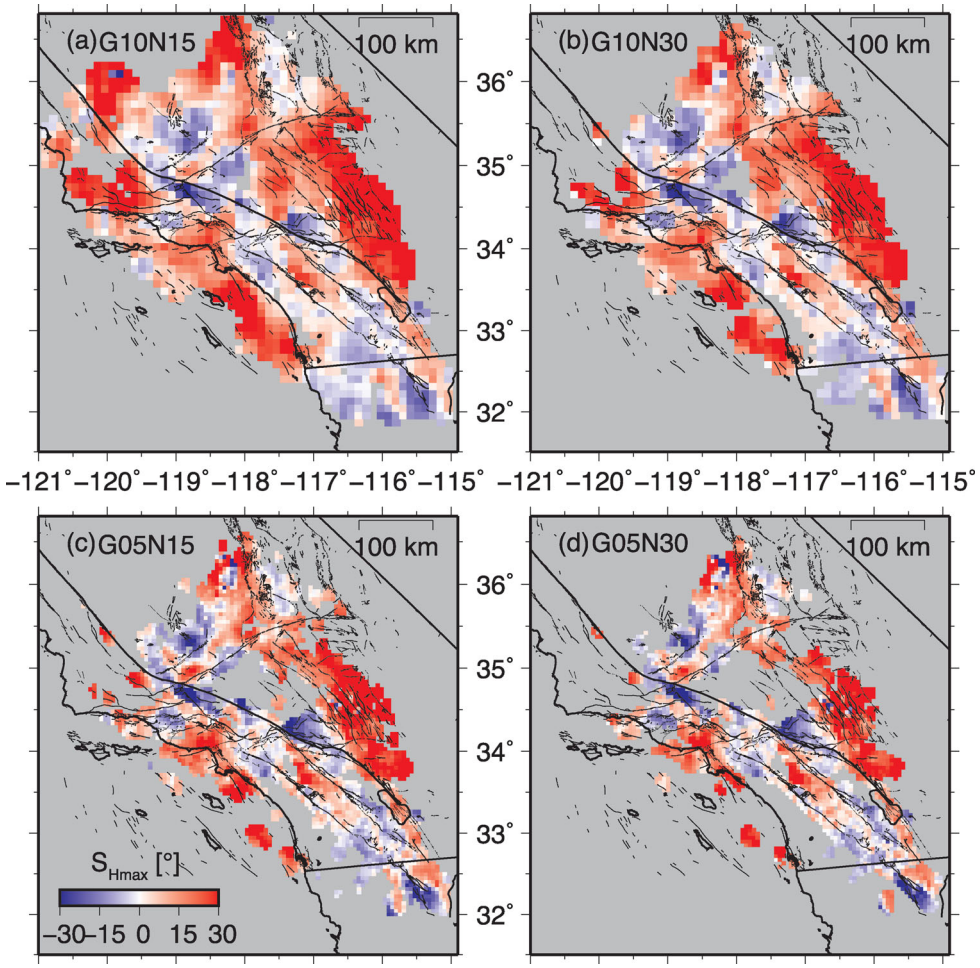

Figure 6. Images of S_{Hmax} trends from 2-D SATSI inversion with (a) grid scale of 10 km and 15 events per grid node (G10N15); (b) grid scale of 10 km and 30 events per grid node (G10N30); (c) grid scale of 5 km and 15 events per grid node (G05N15); (d) grid scale of 5 km and 30 events per grid node (G05N30). The colour legend is at the bottom left-hand side in (c), with orientation relative to the north, and east of north to be positive.

may be related to the heterogeneous post-main shock stress field (Hardebeck & Hauksson 2001b). The style of faulting inside the ECSZ is a mixture of strike-slip and normal faulting (Fig. 10).

3.2.2 *Western Transverse Ranges and Continental Borderland*

The Western Transverse Ranges and Continental Borderland (WTRCB) zone extends to the west of the grey and solid dashed curves ('WPR-L' in Fig. 8), which is located to the west of the SAF inside the Pacific Plate. Except in the Ventura Basin, the S_{Hmax} orientations in this zone are relative homogeneous and range from N20°E as the background level to N40°E close to San Fernando Valley. The style of faulting in this zone is dominated by reverse and strike-slip faulting, which differs from the ECSZ.

Compared with the San Andreas system (discussed in the following section) and the East California Shear Zone, the WTRCB zone has relatively low seismicity rate in these three decades (Hauksson *et al.* 2012). Recent large earthquakes that occurred in WTRCB zone include the 1994 Northridge M_w 6.7 and the 1971 San Fernando M_w 6.6 earthquakes, both of which exhibited reverse faulting. Large strike-slip earthquake could also occur in this zone. For example, the 1933 Long Beach M_w 6.4 earthquake ruptured the NIF (Hauksson & Gross 1991).

3.2.3 *San Andreas system*

With high quality and dense focal mechanism data, local stress heterogeneities of scale length less than 100 km can be resolved in southern California. One general feature of these local stress heterogeneities is that many of them are generally located along the SAF, and another general feature is that the geometrical shapes of these local stress heterogeneities often match with the orientations of neighbouring surface fault traces. Therefore, we identify local stress heterogeneities along the SAF in this section.

There are three pronounced wedge-shaped areas with S_{Hmax} orientated NNW. Two of them lie along the bends in the SAF. One is located to the south of Fort Tejon ['A' in Fig. 8, south of the San Gabriel Fault (SGF) and SAF (in profile F of Fig. 9], and another is located to the east of Cajon Pass ('B' in Fig. 8, and the south edge is close to SAF in profile H of Fig. 9). The sharp boundaries of these two anomalous areas were not well defined in the previous study of Hardebeck & Hauksson (2001b). The third one is located in the branch zone of the Laguna Salada Fault (LSF) to the south of the US-Mexico boundary ('C' in Fig. 8), and was illuminated by the aftershocks of the 2010 M_w 7.0 El Mayor Cucapah earthquake. One common feature of the three wedge-shaped NNW S_{Hmax} areas is that the shapes are relatively sharply defined by neighbouring faults. The wedge A is located in between the SAF and the SGF

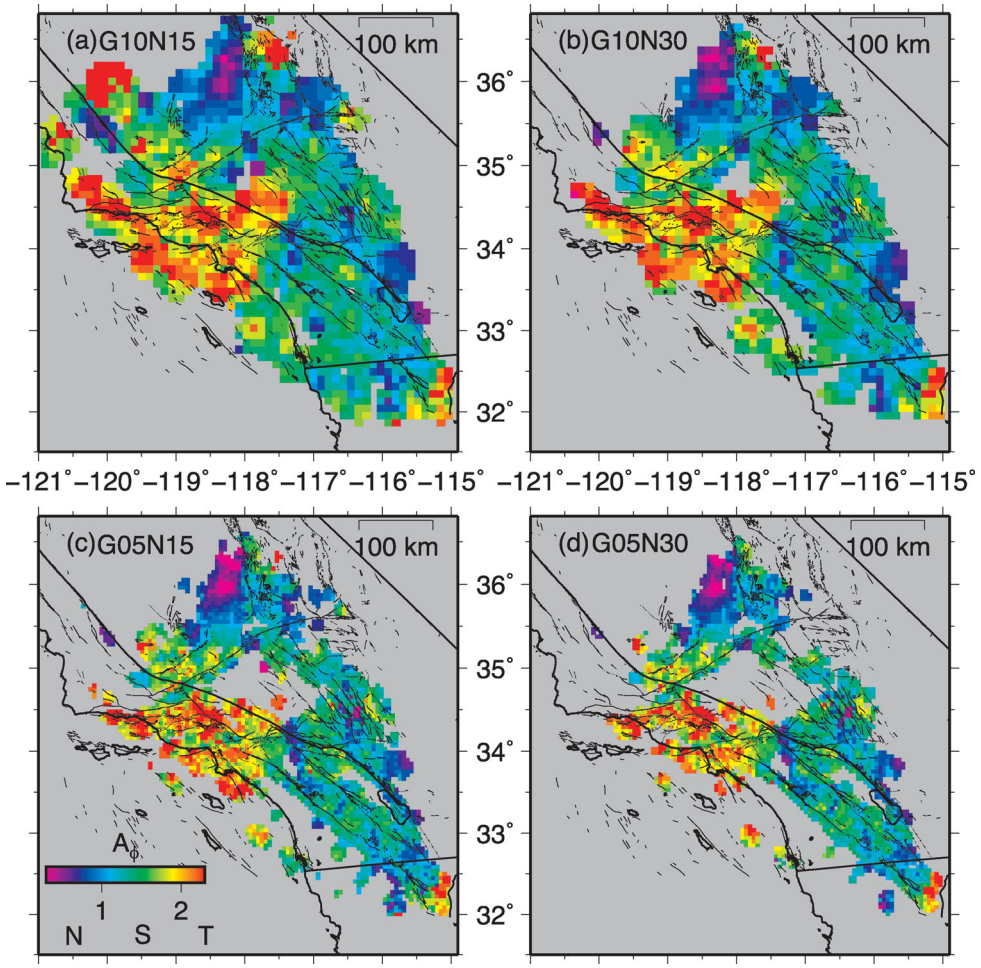

Figure 7. Images of style of faulting (A_ϕ) from 2-D SATSI inversion with (a) grid scale of 10 km and 15 events per grid node (G10N15); (b) grid scale of 10 km and 30 events per grid node (G10N30); (c) grid scale of 5 km and 15 events per grid node (G05N15); (d) grid scale of 5 km and 30 events per grid node (G05N30). The colour legend is at the bottom left-hand side in (c), with normal style of faulting (N) in [0–1], strike-slip style of faulting (S) in [1–2], and reverse style of faulting (T) in beyond 2.0.

with the vertex of the acute angle on the intersection between the SAF and the Garlock Fault (GAF). The wedge B is bounded by the SAF and the Helendale Fault. This wedge has the largest area, and the significance gradually diminishes southward to the vertex of the acute angle. The wedge C is confined in the rupture zone of the LSF.

In between the ECSZ and the WTRCB zones, the background S_{Hmax} orientations are generally in the NS or NNW direction. However, a triangle zone of local stress heterogeneity with S_{Hmax} trending NNE exists in the Anza area ('D' in Fig. 8), and peaks close to the SJF in profiles H and I of Fig. 9. This anomalous area is relatively well confined by neighbouring fault traces, abutting with the SJF to the west. To the north it terminates near where the SAF and the SJF intersect, and to the southwest it generally extends to the Elsinore Fault (ESF).

A broad zone of local stress heterogeneity exists along the Tehachapi Mountains in between the White Wolf Fault (WWF) and the Garlock Fault (GAF), with S_{Hmax} trends in the direction of N20°E ('E' in Fig. 8). Both the WWF and the GAF are left-lateral strike-slip faults, and the 1952 Kern county M_{w}7.3 ruptured the WWF obliquely.

In addition to these local stress heterogeneities listed above, there are NNW stress heterogeneities of smaller spatial extent in the Ventura Basin, the area to the northwest of the WWF.

3.3 Heterogeneities in style of faulting

Several pronounced regional and local heterogeneities are visible in the style of faulting across southern California (Fig. 10).

3.3.1 Convergent bands

There are three distinctive broad curved convergent zones in the Transverse Ranges, extending eastward into the Mojave Desert across the SAF (Fig. 10). The northern most zone ('A' in Fig. 10) is confined by the SAF and the GF to the south. The middle band ('B' in Fig. 10), which is the largest, extends from the Western Transverse Ranges in the west to the middle of Mojave Desert in the east. The middle band is generally located south of the Santa Ynez Fault (SYF in Fig. 1), in the area of the Western Transverse Ranges and San Gabriel Mountains. In general terms, this middle band coincides with the shape of a high *P*-wave velocity anomaly from tomography below the Transverse Ranges (Hadley & Kanamori 1977; Humphreys *et al.* 1984). The southernmost band ('C' in Fig. 10) is mostly south of the Santa Monica Fault (SMF in Fig. 1), and gradually narrows westward within the Continental Borderland. These three convergent bands can also be seen in the profile F in Fig. 11 as distinct zones with higher value of A_ϕ.

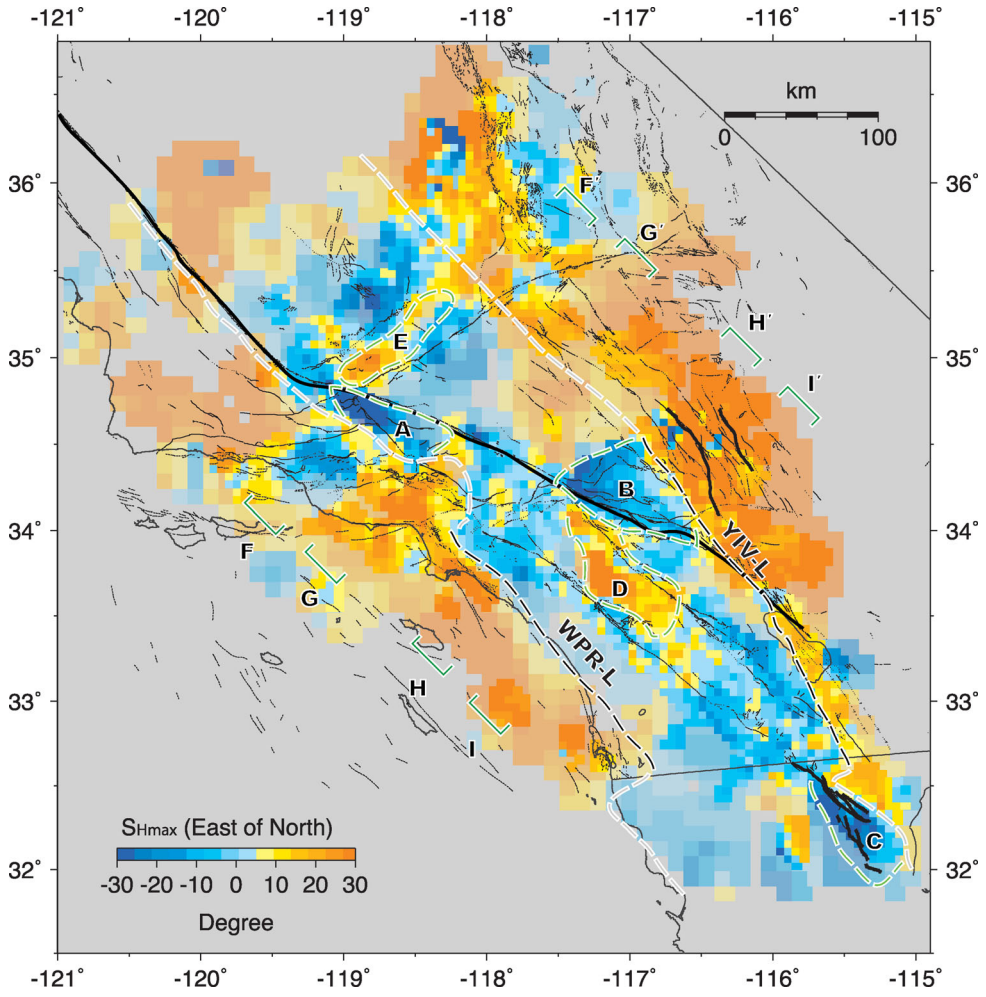

Figure 8. Composite image for S_{Hmax} orientation with overlapping G05N30 above G10N15 (in light colour). The San Andreas Fault, Landers, Hector Mine and El Mayor Cucapah surface ruptures are highlighted in bold black lines. Black dashed lines mark two S_{Hmax} orientation transition lines: the Yucca-Imperial Valleys Line (YIV-L), and the Western Peninsular Ranges Line (WPR-L), respectively. 'A', 'B' and 'C' mark the three identified wedge-shapes (green dashed polygons). 'D' marks isolated NNE S_{Hmax} area (green dashed polygon) along the San Jacinto Fault. 'E' marks the Tehachapi Mountains stress heterogeneity. FF′, GG′, HH′ and II′ are four selected cross-sections with 0.2° in width and 300 km in length. The grey lines are postulated extensions of the WPR-L and the YIV-L as regional stress boundaries in southern California.

3.3.2 Normal faulting zone to the west of SNF

The southern Sierra Nevada, to the west of the SNF and generally to north of the WWF, is dominated by normal faulting ('D' in Fig. 10). Geologically, this zone of normal faulting is located in the western boundary of the Sierra Nevada Mountains, where crustal thinning and high elevation dominate the stress field characteristics and reflect gravitational collapse of the high topography (Unruh *et al.* 2002). As the A_ϕ decreases from south to north (Profile F in Fig. 11), the style of faulting evolves to normal faulting in the southern Sierra Nevada.

3.3.3 San Andreas system

The style of faulting varies along the SAF in different segments from northwest to southeast. To the north, a small zone of normal faulting exists at the Cholame segment along the SAF. Across the Tejon Pass, reverse faulting dominates the faulting style from Wheeler Ridge to the north side of the GAF, and strike-slip faulting dominates from the south side of the GAF to the SYF. In the middle of the Mojave segment, reverse faulting dominates on both sides of the SAF. To the south of Cajon Pass, a notable north-south elongated area with dominant normal faulting exists ('E' in Fig. 10, corresponding to low values of A_ϕ in between SJF and SAF in profile G in Fig. 11). One important tectonic feature of this area is that it is in where the SJF emerges and branches from the SAF southward. There is no correspondingly confining fault trace at the boundaries to this normal faulting anomaly. Further southeastward, the stress regime mostly corresponds to strike-slip faulting along the SAF until it comes to the Coachella Valley, where the SAF terminates, and normal faulting prevails (Fig. 10).

4 INTERPRETATIONS OF S_{Hmax} AND OTHER DEFORMATION FIELDS

In this section, using results with the best resolution (G05N30), we compare the horizontal stress field with horizontal stress field orientations determined from other geophysical techniques in southern California.

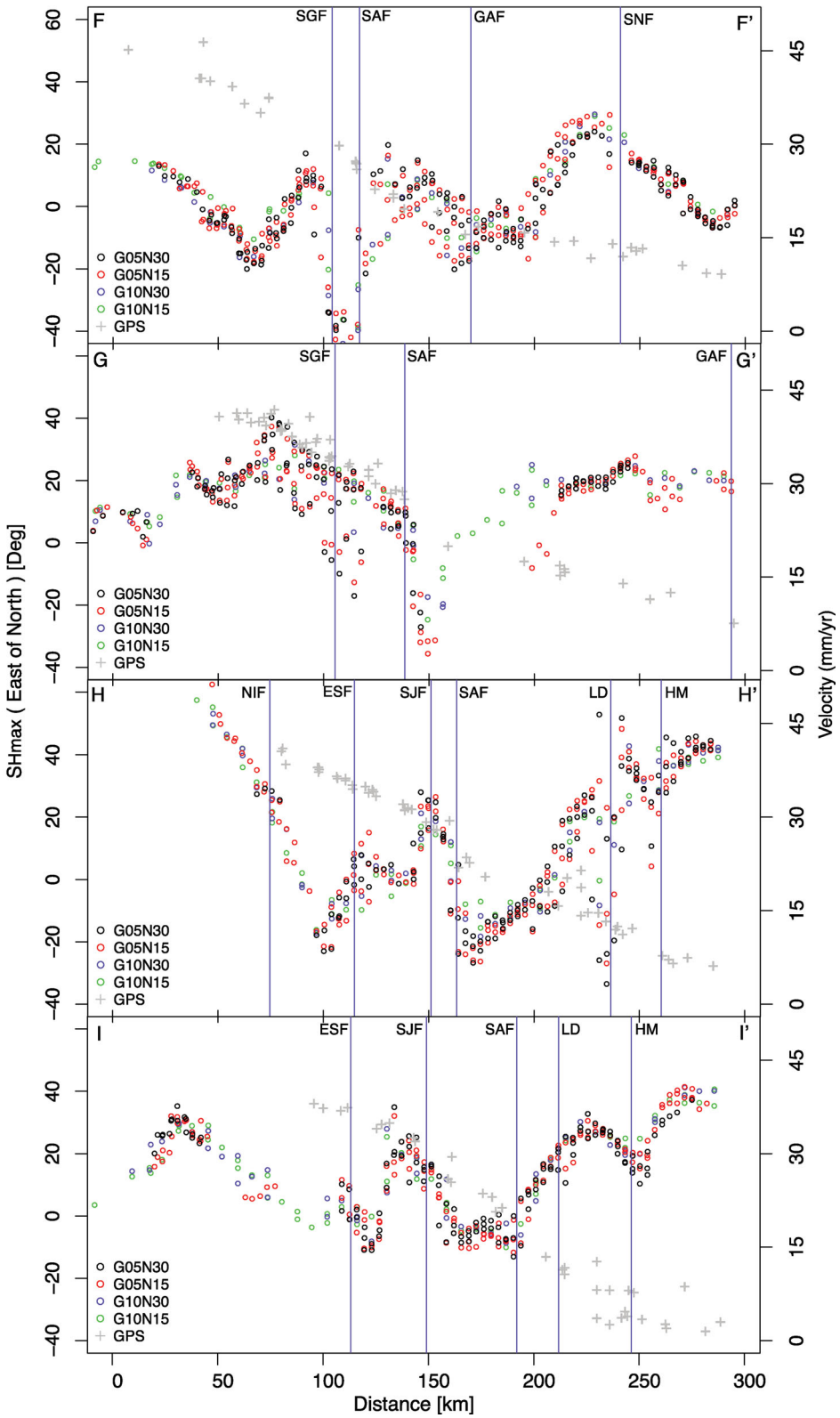

Figure 9. Orientations of S_{Hmax} from four inversion schemes along selected profiles in Fig. 8. Grey crosses mark GPS velocities of stations inside each profile. ESF, Elsinore Fault; GAF, Garlock Fault; HM, Hector Mine rupture; LD, Landers rupture; NIF, Newport-Inglewood Fault; SAF, San Andreas Fault; SGF, San Gabriel Fault; SNF, Sierra Nevada Fault; SJF, San Jacinto Fault.

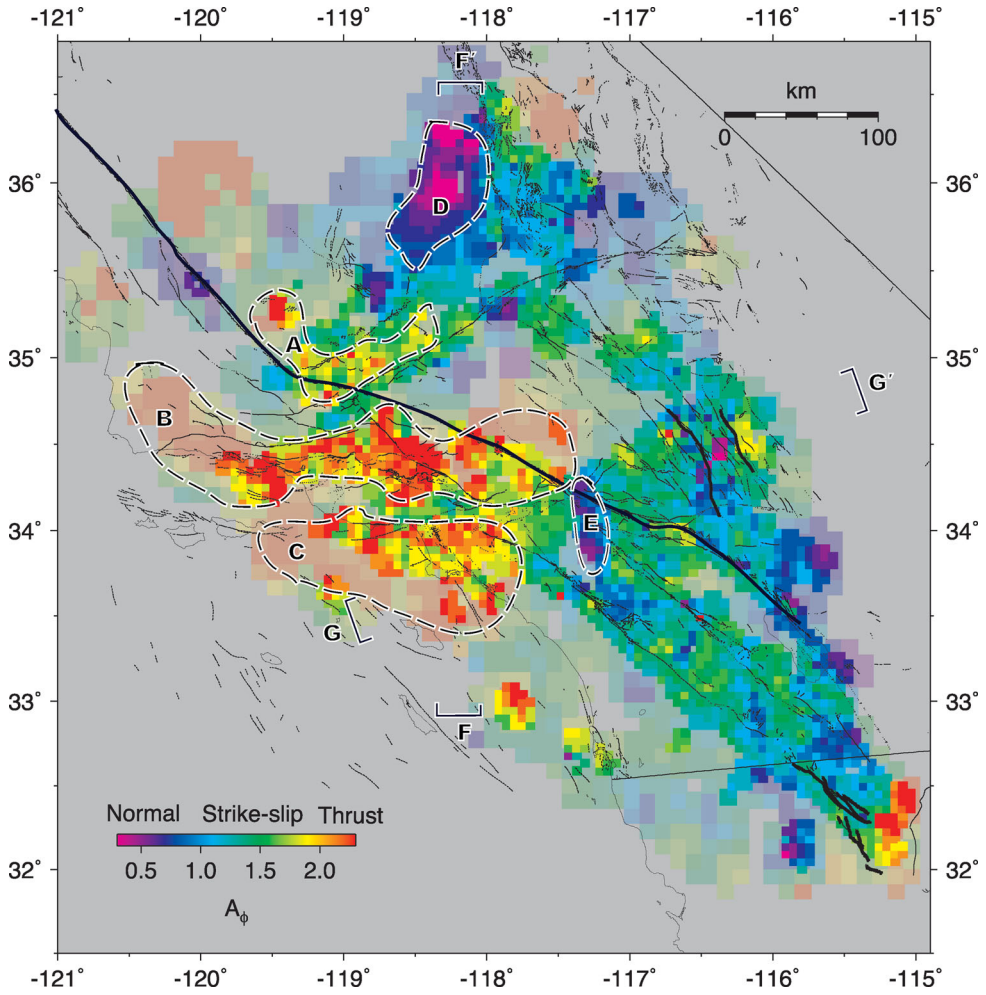

Figure 10. Composite image for the style of faulting (A_ϕ) with overlapping G05N30 above G10N15 (in light colour). The San Andreas Fault, Lander, Hector Mine, and El Mayor Cucapah surface ruptures are highlighted in bold black lines. 'A', 'B' and 'C' mark the three identified convergent bends. 'D' marks the Normal Faulting Zone to the east of Sierra Nevada Fault. 'E' marks the NS Normal Faulting Stripe in San Bernardino Mountains. FF′ and GG′ are two selected profiles, 0.2° wide and 300 km long.

4.1 GPS strain orientations

We compare S_{Hmax} orientations with the axis of the maximum shortening strain rate tensor ($\dot{\varepsilon}_3$), similar to Townend & Zoback's (2006) analysis of Japanese data. To determine $\dot{\varepsilon}_3$, we use the horizontal strain rate tensor field for southern California on 0.1° × 0.1° scale as calculated by Holt *et al.* (2010). We calculate the second invariant of strain rate (Fig. 12), and the trends of the axes of horizontal strain rate tensors.

For each grid node with a S_{Hmax} orientation, we use the nearest $\dot{\varepsilon}_3$ orientation within 10 km distance, and calculate the angular difference to the S_{Hmax} orientation. Because the uncertainties of $\dot{\varepsilon}_3$ orientations correlate with the magnitude of the strain rate, we scale the $\dot{\varepsilon}_3$ orientations and associated angular difference with the second invariant of strain rate (Fig. 13). We compare these angular differences with the uncertainties in the S_{Hmax} orientations, and find no correlation. Generally, both orientations match within 30°, and orientations of S_{Hmax} trend more eastward than the orientations of $\dot{\varepsilon}_3$, especially along the SAF, along the SJF to the north of Anza and in the ECSZ. In contrast, the trend of S_{Hmax} is more westward in the Salton Trough and the Imperial Valley. On a local scale, the GPS strain rate tensor field does not capture the anomalous NNE S_{Hmax} trend near Anza ('D' in Fig. 8). In addition, there is a relatively large discrepancy in the East Los Angeles (ELA) area, between the Los Angeles basin and the San Gabriel Mountains, where the orientation of $\dot{\varepsilon}_3$ is closer to EW direction while the orientation of S_{Hmax} trends generally NS (Fig. 13).

Townend & Zoback (2006) reported large angular discrepancies between S_{Hmax} and $\dot{\varepsilon}_3$ in central Japan, and they attributed the discrepancies to localized mountain building related with crustal collision. Yang & Hauksson (2011) showed that the ELA area exhibits strong vertical strain partitioning with the S_{Hmax} orientation rotating from N12°W at shallow depth to due north at the bottom of the seismogenic zone. The escape tectonics that are associated with north–south thrusting in the middle crust and east–west extension in the upper crust (Walls *et al.* 1998) may explain the proximity of the two deformation fields.

4.2 Upper-mantle anisotropy orientations

Because mantle convection serves as the driving force for plate tectonics, we compare the orientations of the stress and strain fields with upper-mantle anisotropy beneath in southern California. Seismic anisotropy observations from shear wave (SKS) splitting have been used to infer material deformation in the upper mantle (e.g.

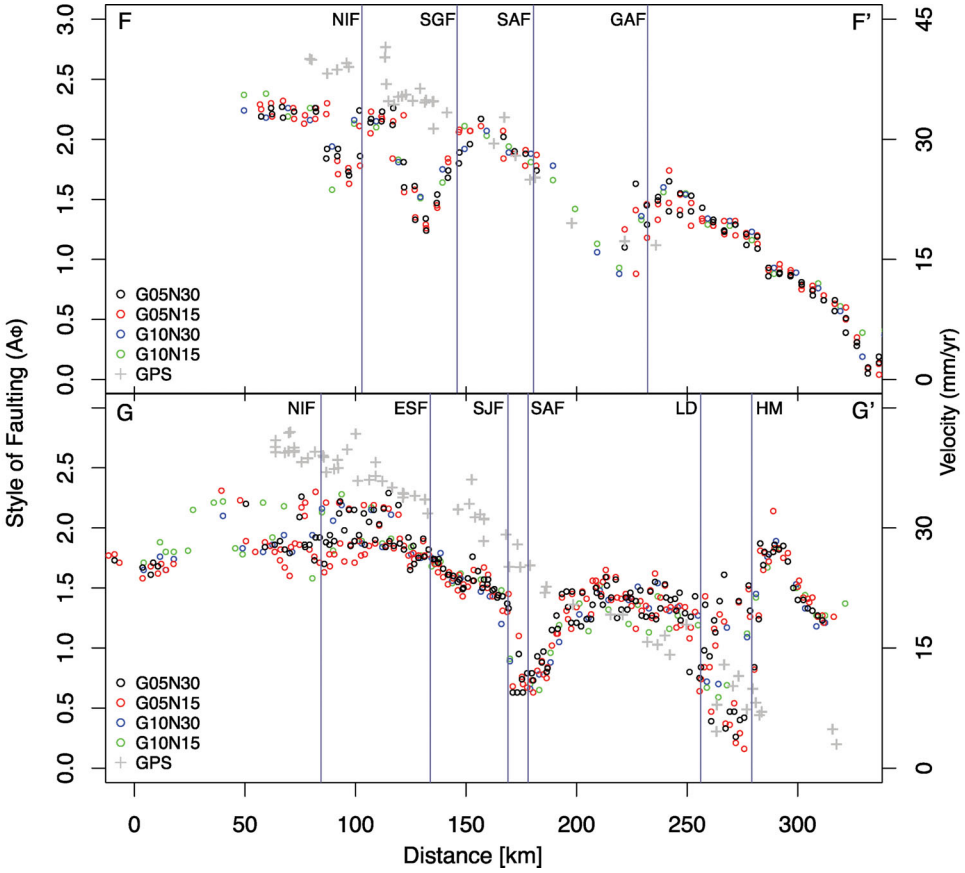

Figure 11. Style of faulting (A_ϕ) profiles from four inversion schemes along selected profiles in Fig. 10. GPS velocities of stations inside each profile are marked by symbols in grey cross. ESF, Elsinore Fault; GAF, Garlock Fault; HM, Hector Mine rupture; LD, Landers rupture; NIF, Newport-Inglewood Fault; SAF, San Andreas Fault; SGF, San Gabriel Fault; SJF, San Jacinto Fault.

Silver 1996; Savage 1999). Polet & Kanamori (2002) showed that the fast directions of seismic anisotropy derived from SKS wave are uniform, and are generally orthogonal to the direction of S_{Hmax} in southern California. Using a subset of 191 SKS upper-mantle anisotropy data for southern California, which are available from the shear wave splitting database assembled by Wüstefeld *et al.* (2009), we compare the S_{Hmax} orientations with anisotropy orientations in the slowest directions. For each station with available anisotropy measurements, we use the nearest S_{Hmax} within a distance of 10 km. We obtain results for 152 pairs of data points, and the differences with associated S_{Hmax} orientations are generally within 60° (Fig. 14). Since the SKS splitting database (Wüstefeld *et al.* 2009) is a collection of results measured by different authors using different methods, for some stations with multiple measurements, the reported anisotropy orientations could differ by 10°–60°. As a result, the uncertainties in anisotropy orientations could somewhat contribute to the relative large angular difference between the two fields. Nevertheless, for the first order approximation, the S_{Hmax} orientations are systematically rotates eastwards relative to the anisotropy orientations in the upper mantle (Fig. 14).

The distributions of trends of stress, strain, and anisotropy have different Gaussian shapes, with the average orientation of the maximum shortening axis of N4°E at the surface based on GPS strain rate tensor, N7°E in the crust based on stress inversion from focal mechanisms, and N7°W in the upper mantle based on anisotropy (Fig. 15). The distribution of strain has two peaks, with one coinciding with the S_{Hmax} and the other overlapping with the dominant orientation of anisotropy in the upper mantle. Thus the GPS measured strain field captures both the stress in the seismogenic crust as well as the deformation field of the upper-mantle anisotropy.

5 DISCUSSIONS

5.1 New insights into tectonics from S_{Hmax}

Horizontal movements that dominate the tectonics in the Pacific North American Plate boundary (e.g. GPS velocity field, style of faulting), and the differential movements between neighbouring faults in the fault system produce heterogeneities in the orientation of S_{Hmax}. The high-resolution distribution of S_{Hmax} trends reveals two sharp regional transitional boundaries along the Pacific-North America Plate boundary in southern California. These two boundaries limit the east-west lateral extent of the San Andreas system.

The Yucca-Imperial Valleys Line (YIV-L) is a sharp S_{Hmax} orientation boundary that trends north-northwest across the eastern part of southern California (Fig. 8). The YIV-L that starts from the Yucca Valley in the Mojave Desert trends south–southeast, subparallel to the SAF, into Coachella Valley, and runs across the Salton Trough and the Imperial Valley towards the U.S.–Mexico border for a distance of 250 km. East of the YIV-L, the trends of S_{Hmax} are generally in N20°E-N40°E (Profiles G, H and I in Fig. 9), while the orientations of S_{Hmax} to its west are generally in the NS or NNW direction. Both the rupture zones of the 1992 M_{w} 7.4 Landers earthquake and the 1999 M_{w} 7.1 Hector Mine earthquake (bold black

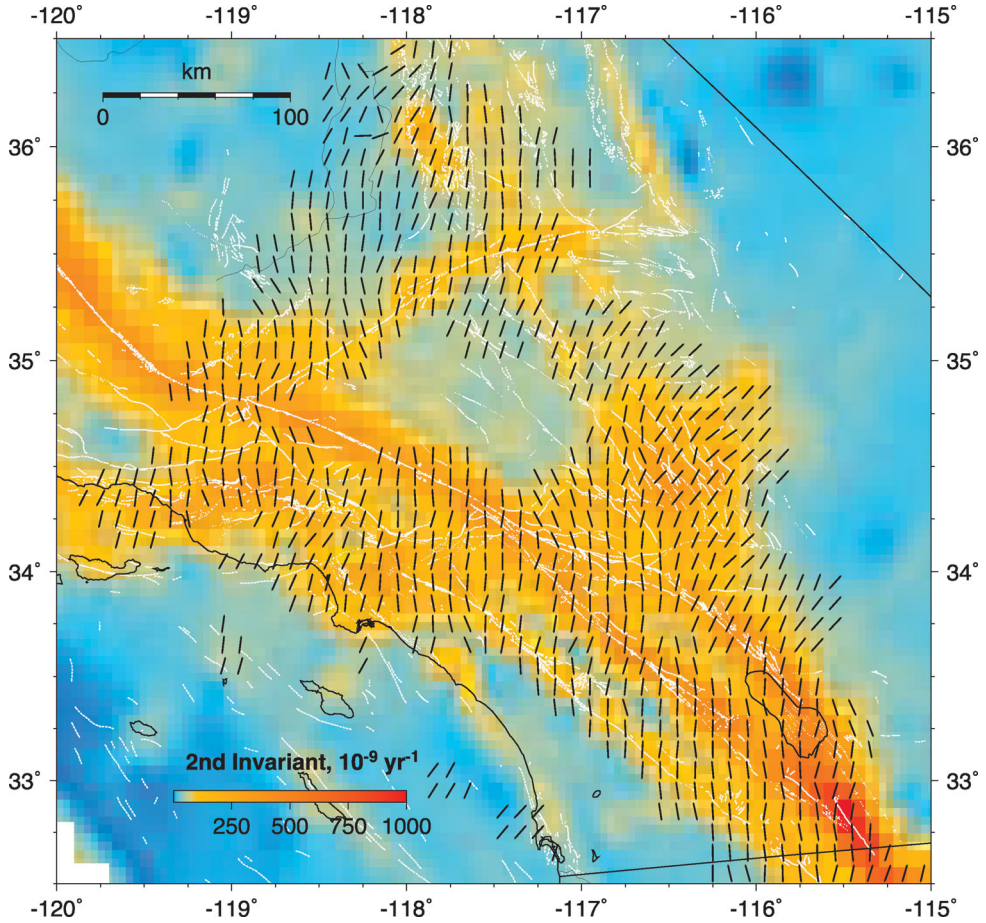

Figure 12. Orientations of S_{Hmax} on the image of strain rate (Holt *et al.* 2010). Fault traces mapped by Jennings (1994) are in white. S_{Hmax} orientations of G05N30 are overprinted (black bars, data are down-sampled for the purpose of visualization). Strain rate are coloured by the second invariant with legend at the bottom left-hand corner.

curves in Fig. 8) are located on the east side of the YIV-L (profile H in Fig. 9).

Following the trend of this stress transition, a natural extension of the YIV-L could extend to the northwest into the Central Valley (grey dashed curve) in Fig. 8, and step westward and extend southeastward in the Baja California. It has been proposed that the ECSZ, together with the Walker Lane in central to northern California and Nevada could be in the progress of forming a new plate boundary (e.g. Nur *et al.* 1993; Wesnousky 2005). However, both the M_w 7.3 Landers and M_w 7.1 Hector Min earthquake occurred to the east of the YIV-L, making its role in the long-term plate boundary migration unclear.

Another sharp S_{Hmax} orientation boundary follows the Western Peninsular Ranges Line (WPR-L), subparallel to the NIF, and extends south-southeast in a relatively straight line to the US-Mexico border (Fig. 8). The orientation of S_{Hmax} is generally in a N20°E–N40°E direction west of this line (Profiles G and H in Fig. 9), and in a NS or NNW direction east of this line. Following the stress orientation transition boundary, a natural extension of the WPR-L could extend northward circling around the San Fernando Valley, and continue northwest to be parallel to the SAF in central California (grey dashed curve).

The SAF in southern California is commonly regarded as a weak fault, with the trends of S_{Hmax} forming high angles to the SAF trace (e.g. Jones 1988; Mount & Suppe 1992). Hardebeck & Hauksson (1999) found that the angle between S_{Hmax} orientations and the SAF in southern California decreases from high angle (~60°) at far field to low angle (~40°) near the fault with in 10–20 km. The high-resolution image of S_{Hmax} orientations in this study (Fig. 8) shows much more detail than was presented by Hardebeck & Hauksson (1999). Outside of the WPR-L and the YIV-L, the background S_{Hmax} orientations are generally in a NNE direction. However, in between the two lines, the background S_{Hmax} orientations are generally in a NNW–NS direction. These observations conform to Hardebeck & Hauksson (1999) in that the angle between S_{Hmax} orientations and the SAF generally decreases from far field to near field. However, the stress heterogeneities along the SAF exhibit more complex and spatially asymmetric patterns. Instead of being symmetrically distributed along major faults, the localized stress heterogeneities ('A', 'B', 'C', 'D' and 'E' in Fig. 8) form asymmetric patterns adjacent to major faults, and the zones of heterogeneity are in generally delimited by neighbouring major faults.

Confined in between the YIV-L and the WPR-L, the San Andreas system in southern California is essentially a broad shear zone (~150 km in width) characterized by strong stress heterogeneity. Numerical simulations of such a system revealed similar patterns showing that the stress field is relatively homogeneous outside of the shear zone and is much more heterogeneous within it (Scott 1996). To favour large deviations in stress orientations inside the San Andreas system, lower deviatoric stress and a high level of pore fluid pressure are required (Faulkner *et al.* 2006).

Block rotations controlled by active faulting have been reported and explained by different authors (Freund 1970; Garfunkel 1974;

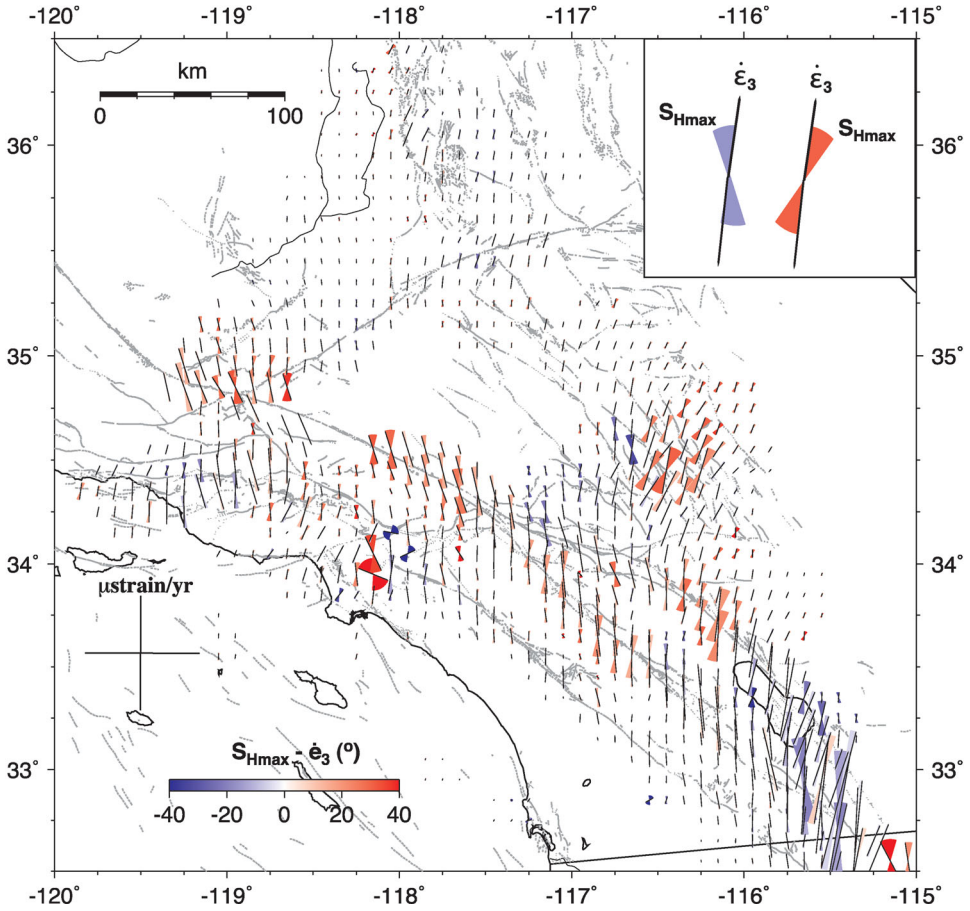

Figure 13. Rotational wedges illustrating the angular difference between the orientations of S_{Hmax} and the maximum compressive strain rate axis ($\dot{\varepsilon}_3$) derived from GPS measurements (Holt *et al.* 2010) in southern California. The orientations of $\dot{\varepsilon}_3$ are in lines in black, and scaled by strain rate with legend at the bottom left-hand side. The angular differences from S_{Hmax} orientations to $\dot{\varepsilon}_3$ orientations are coloured with legend at the bottom left-hand side. Pair of examples is illustrated in the top right-hand corner.

Ron *et al.* 1984; Nicholson *et al.* 1986; Nur *et al.* 1986; Jackson & Molnar 1990). Block rotations may cause the formation of local S_{Hmax} heterogeneities as movement occurs on multiple faults at high angles to each other.

By assuming that the local S_{Hmax} heterogeneities are solely caused by active faulting, we can provide a simple explanation (similar to that of Freund 1970) for the origin of several local stress heterogeneities ('A', 'B' and 'E' in Fig. 8). As shown in Fig. 16, in the broad right-lateral shear band of southern California, the SAF bends from the WPR-L to the YIV-L forming two wedge-shaped areas close to the Tejon Pass and Cajon Pass, respectively. With both sides confined by right-lateral strike-slip faulting, the two wedges tend to rotate counter-clockwise. Consequently, the local S_{Hmax} trends in 'A' and 'B' are more towards the NNW as compared to the regional S_{Hmax} orientations towards the NNE. The Tehachapi Mountains are located in between two left-lateral strike-slip faults: the WWF and the GAF. With the continuous motions of the neighbouring active faults, the local S_{Hmax} trends in the Tehachapi Mountains rotate clockwise from NS to NNE. Local stress heterogeneities in the Cucapah Range ('C' in Fig. 8) could also be explained similarly. However, this model cannot explain the NNE stress heterogeneity pattern in the northern part of the SJF ('D' in Fig. 8), which is confined between two right-lateral strike-slip faults (SJF and ESF). One possible explanation for the origin of this stress heterogeneity could be the differential movement of adjacent faults. As the fault slip rate for the SJF is significantly faster than it is for the ESF (Meade & Hager 2005), the block in between these two faults essentially follows simple shear deformation (Fig. 16), and consequently the S_{Hmax} orientation inside the block rotates clockwise. Our tectonic model that is based on both focal mechanisms and GPS measurements provides more details about crustal deformation in southern California than was available before. However, future data may provide further refinements of our model.

5.2 Crustal thickening and thinning from style of faulting

Compared with heterogeneities in S_{Hmax} orientations, which are mainly controlled by horizontal geometrical complexities in the plate boundary, the heterogeneities in the style of faulting are more related to the vertical deformation associated with crustal thickening and thinning.

To accommodate the regional S_{Hmax} orientations to the NNE, the crustal shortening in southern California is accompanied by EW extrusion in the Transverse Ranges with multiple left-lateral strike-slip faults (e.g. the SYF, the SMF), and by NS crustal thickening with the existence of three convergent bands ('A', 'B' and 'C' in Fig. 10). Geological evidence shows that the Mojave Block has undergone significant late Cenozoic NS contraction (Bartley *et al.* 1990). In addition, there are subsurface blind thrust fault

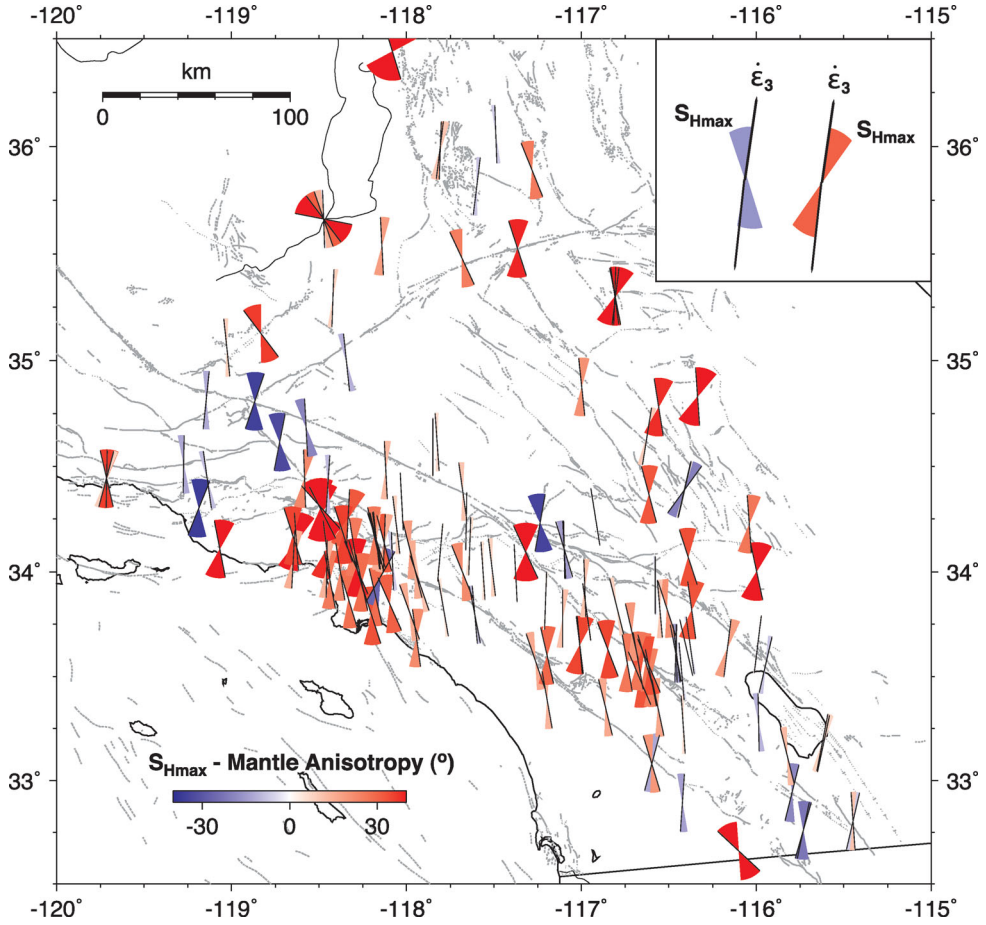

Figure 14. Rotational wedges illustrating the angular difference between the azimuths of the maximum horizontal compressive stress (S_{Hmax}) in the crust and the slowest directions of anisotropy in the upper mantle beneath southern California. The orientations of Anisotropy in upper mantle are in lines in black. The angular differences from S_{Hmax} orientations to anisotropy orientations are coloured with legend at the bottom left-hand side. Pair of examples is illustrated in the top right-hand corner.

systems (Shaw & Shearer 1999). Geomorphically, the largest convergent band ('B' in Fig. 10) coincides with the high-velocity upper-mantle anomalies (Hadley & Kanamori 1977; Humphreys *et al.* 1984). If the lithospheric deformation is vertically overlapping over a wide range of depth, one reasonable link between them is could be gravitational sinking, which pulls the crust downward (Hearn & Clayton 1986).

To the north of the convergent bands, the A_ϕ value drops to below 1.0 (FF′ in Fig. 11), and the style of faulting becomes more heterogeneous in the Sierra Nevada ('D' in Fig. 10). Unruh *et al.* (2002) attributed this to the gravitational collapse in the Sierra Nevada, which produces a zone of crustal extension with mostly normal faulting. To the east of the convergent bands, the crustal deformation is in the state of transtension within the Basin and Range Province, characterized by strike-slip faulting and normal faulting. The divergence of the San Jacinto Fault from the SAF generates a local heterogeneity in style of faulting with predominate normal faulting ('E' in Fig. 10 and profile GG′ in Fig. 11). The occurrence of the Landers (1992) and Hector Mine (1999) earthquakes triggered many aftershocks with normal faulting, and generated a local area with marked heterogeneity in style of faulting between the two ruptures (Profile GG′ in Fig. 11). Further south, from the Peninsular Ranges to the Imperial Valley, strike-slip faulting and normal faulting co-exist. This reflects crustal thinning related to rift spreading. As a rift zone, the Salton Trough region is experiencing lithospheric thinning (Lekic *et al.* 2011), characterized by high heat flow and conjugate seismicity patterns.

5.3 Crustal and upper-mantle deformation processes

Models such as small-scale sublithospheric convection in southern California have been proposed (Humphreys *et al.* 1984; Schmandt & Humphreys 2010) to explain the existence of crustal thickening in the Transverse Ranges and crustal thinning in the Salton Trough rifting zone. If sublithopheric convection between the Transverse Ranges and the Salton Trough exists, the multiple thrust convergent bands and the upper-mantle density anomalies may be required to accommodate convective flow in the NNW direction. Furthermore, the upper-mantle flow direction in southern California is generally in an EW direction (Polet & Kanamori 2002; Silver & Holt 2002), which may interact with the perturbation associated with small-scale upper-mantle convection, and thus form multiple convergent zones.

In this study, we find that the S_{Hmax} orientation in the seismogenic layer is rotated about 14° clockwise relative to the maximum shortening direction indicated by anisotropy in the upper mantle. The observation of a small rotational angle between the two layers in the maximum horizontal compressional or shortening direction, favours a relatively strongly coupled lithosphere in southern

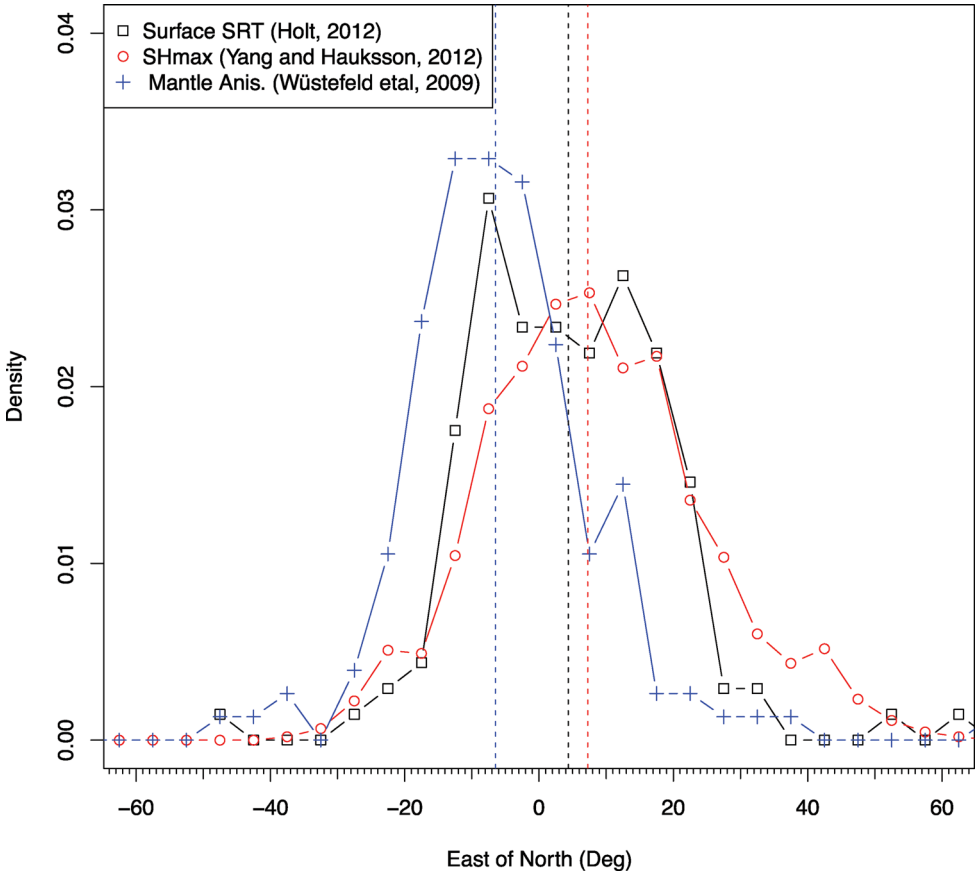

Figure 15. Histograms of the orientations of the principal horizontal shortening axes from surface strain rate tensor (SRT; Holt *et al.* 2010), stress tensors inverted from earthquake focal mechanisms (this work), and Anisotropy database (Wüstefeld *et al.* 2009) in southern California. For each distribution, the mean value is marked by vertical dashed line, with N4°E, N7°E and N7°W for the orientation of the maximum horizontal compressive axes on the surface, in the crust, and in the upper mantle, respectively.

California (Bird & Kagan 2004). Comparison between upper-mantle flow and surface GPS motion in an active tectonic region between Tibet and southern Asia by Wang *et al.* (2008) also reveals that crust and upper-mantle deform coherently.

The GPS maximum shortening strain rate tensor ($\dot{\varepsilon}_3$) orientations exhibit an intermediate distribution between the distribution of upper-mantle maximum shortening directions and distribution of S_{Hmax} orientations (Fig. 15). While mostly overlapping with the distribution of S_{Hmax} orientations, the $\dot{\varepsilon}_3$ distribution shares its peak with the distribution of upper-mantle maximum shortening directions. This indicates that the GPS observations capture some of the upper-mantle deformation field, as well as the deformation in the seismogenic zone.

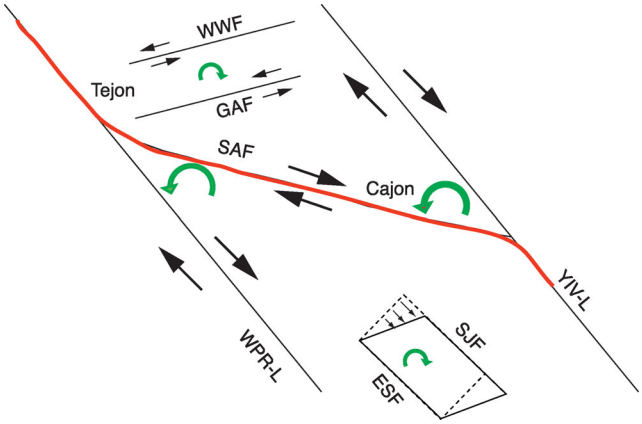

Figure 16. Illustration of one possible explanation for the origin of stress heterogeneities associated with active faulting. ESF, Elsinore Fault; GAF, Garlock Fault; SAF, San Andreas Fault; SJF, San Jacinto Fault; WWF, White Wolf Fault; YIV-L, the Yucca-Imperial Valleys Line; WPR-L, the Western Peninsular Ranges Line.

6 CONCLUSIONS

We obtained high-resolution images for the orientation of the stress field and style of faulting in southern California by using a catalogue of high-quality earthquake focal mechanisms from 1981 to 2010. The S_{Hmax} orientation images are in scale from 5 to 10 km, with 1σ uncertainty in 11°. Our results are generally consistent with previous results of Hardebeck & Hauksson (2001b), but with more data and better spatial coverage, our results reveal regional and local spatial heterogeneities in the stress field at a higher resolution.

From the S_{Hmax} orientation images, the southern California region can be generally divided into three subparallel zones separated by two sharp lines across which the stress field changes (the YIV Line and the WPR Line). The Eastern California Shear Zone to the east, and the Continental Borderland and the Western Transverse Ranges Zone to the west have relatively homogeneous S_{Hmax} orientations trending due NNE, which match with the regional S_{Hmax} orientations pattern in California. The SAF system in the middle,

with background S_{Hmax} orientations of NS–NNW, includes multiple local stress heterogeneities. Often the shapes of the local stress patterns change abruptly at the surface traces of major faults.

The local heterogeneities in the S_{Hmax} orientations are likely to be localized along the San Andreas system, and include NNW trends along the SAF near Cajon Pass, Tejon Pass, and the Cucapah Range, as well as NNE trends near the northern San Jacinto Fault and the Wheeler Ridge region.

The style of faulting exhibits similar complexity, ranging from predominantly normal faulting in the high Sierra Nevada, to strike-slip faulting along the San Andreas system, to three consecutive bands of thrust faulting in the Wheeler Ridge area and the Western Transverse Ranges. The local variations in the style of faulting include normal faulting at the north end of the San Jacinto fault and scattered regions of thrust faulting.

We compare the S_{Hmax} orientations, the orientation of the maximum shortening axes ($\dot{\varepsilon}_3$), and orientations of the mantle shear wave anisotropy. The distribution of S_{Hmax} orientations is closer to the trend of the $\dot{\varepsilon}_3$ than to the trend of the mantle anisotropy. The mean trend of S_{Hmax} lies about 14° clockwise of the trend of the maximum shortening directions of anisotropy in the upper mantle.

Active faulting contributes to the local stress heterogeneities. Other tectonic processes such as gravitational sinking and collapse influence the regional and local style of faulting heterogeneities.

ACKNOWLEDGEMENTS

We thank the personnel of the USGS/Caltech Southern California Seismic Network (SCSN) who pick arrival times and archive the seismograms and the Southern California Earthquake Data Center (SCEDC) for distributing the data. Funding for this research was provided by NEHRP/USGS grant 12HQPA0001. This research was also supported by the Southern California Earthquake Center, which is funded by NSF Cooperative Agreement EAR-0106924 and USGS Cooperative Agreement 02HQAG0008. This is SCEC contribution 1677 and contribution number 10082, Seismological Laboratory, Division of Geological and Planetary Sciences, California Institute of Technology, Pasadena. We appreciate Jeanne Hardebeck and Andy Michael for making the SATSI program available. We appreciate Carl Tape for useful discussions on strain rate tensor, and William Holt for providing strain rate tensor results for southern California. We appreciate Joann Stock for valuable comments and suggestions. We appreciate editor Saskia Goes and two anonymous reviewers for constructive comments and valuable suggestions.

REFERENCES

Angelier, J., 1979. Determination of the mean principal directions of stressesfor a given fault population, *Tectonophysics,* **56,** T17–T26.

Angelier, J., 1984. Tectonic analysis of fault slip data sets, *J. geophys. Res.,* **89,** 5835–5848.

Bartley, J.M., Glazner, A.F. & Schermer, E.R., 1990. North-south contraction of the Mojave block and strike-slip tectonics in southern California, *Science,* **248,** 1398–1401.

Bird, P. & Kagan, Y.Y., 2004. Plate-tectonic analysis of shallow seismicity; apparent boundary width, beta, corner magnitude, coupled lithosphere thickness, and coupling in seven tectonic settings, *Bull. seism. Soc. Am.,* **94,** 2380–2399.

Bott, M.H.P., 1959. The mechanics of oblique slip faulting, *Geol. Mag.,* **96,** 109–117.

Ellsworth, W.L. & Zhonghuai, X., 1980. Determination of the stress tensor from focal mechanism data (abstract), *EOS, Trans. Am. geophys. Un.,* **61,** 1117.

Faulkner, D.R., Mitchell, T.M., Healy, D. & Heap, M.J., 2006. Slip on "weak" faults by the rotation of regional stress in the fracture damage zone, *Nature,* **444,** 922–925.

Freund, R., 1970. Rotation of strike-slip faults in Sistan, southeast Iran, *J. Geol.,* **78,** 188–200.

Garfunkel, Z., 1974. Model for the late Cenozoic tectonic history of the Mojave Desert, California, and for its relation to adjacent regions, *Geol. Soc. Am. Bull.,* **85,** 1931–1944.

Gephart, J.W. & Forsyth, D.W., 1984. An improved method for determining the regional stress tensor using earthquake focal mechanism data: application to the San Fernando earthquake sequence, *J. geophys. Res.,* **89,** 9305–9320.

Hadley, D. & Kanamori, H., 1977. Seismic structure of the Transverse Ranges, California, *Geol. Soc. Am. Bull.,* **88,** 1469–1478.

Hardebeck, J.L. & Hauksson, E., 1999. Role of fluids in faulting inferred from stress field signatures, *Science,* **285,** 236–239.

Hardebeck, J.L. & Hauksson, E., 2001a. Stress orientations obtained from earthquake focal mechanisms: what are appropriate uncertainty estimates? *Bull. seism. Soc. Am.,* **91,** 250–262.

Hardebeck, J.L. & Hauksson, E., 2001b. The crustal stress field in southern California and its implications for fault mechanics, *J. geophys. Res.,* **106,** 21 859–21 882.

Hardebeck, J.L. & Michael, A.J., 2006. Damped regional-scale stress inversions: methodology and examples for southern California and the Coalinga aftershock sequence, *J. geophys. Res.,* **111,** B11310, doi:10.1029/2005JB004144.

Hardebeck, J.L. & Shearer, P.M., 2002. A new method for determining first-motion focal mechanisms, *Bull. seism. Soc. Am.,* **92,** 2264.

Hardebeck, J.L. & Shearer, P.M., 2003. Using S/P amplitude ratios to constrain the focal mechanisms of small earthquakes, *Bull. seism. Soc. Am.,* **93,** 2434–2444.

Hartse, H., Fehler, M., Aster, R. & Scott, J., 1994. Small-scale stress heterogeneity in the Anza seismic gap, southern California, *J. geophys. Res.,* **99,** 6801–6818.

Hauksson, E., Yang, W. & Shearer, P.M., 2012. Waveform relocated earthquake catalog for Southern California (1981 to June 2011), *Bull. seism. Soc. Am.,* **102,** 2239–2244.

Hauksson, E. & Gross, S.J., 1991. Source parameters of the 1933 Long Beach earthquake, *Bull. seism. Soc. Am.,* **81,** 81–98.

Hearn, T.M. & Clayton, R.W., 1986. Lateral velocity variations in Southern California. II. Results for the lower crust from Pn waves, *Bull. seism. Soc. Am.,* **76,** 511–520.

Heidbach, O., Tingay, M., Barth, A., Reinecker, J., Kurfeß, D. & Müller, B., 2010. Global crustal stress pattern based on the World Stress Map database release 2008, *Tectonophysics,* **482,** 3–15.

Holt, W.E., Klein, E. & Flesch, L.M., 2010. GPS strain rates, optimal fault slip rates, and predicted moment rates in Western U.S. Plate Boundary Zone, in *Proceedings of the Workshop on Incorporating Geodetic Surface Deformation Data into UCERF3* Palm Spring, California.

Humphreys, E., Clayton, R.W. & Hager, B.H., 1984. A tomographic image of mantle structure beneath southern California, *Geophys. Res. Lett,* **11,** 625–627.

Jackson, J. & Molnar, P., 1990. Active faulting and block rotations in the western Transverse Ranges, California, *J. geophys. Res.,* **95,** 22 073–22 087.

Jennings, C.W., 1994. Fault activity map of California and adjacent areas, with locations and ages of recent volcanic eruptions, *Calif. Div. Mines and Geology,* Geologic Data Map No. 6, map scale 1:750,000.

Jones, L.M., 1988. Focal mechanisms and the state of stress on the San Andreas fault in southern California, *J. geophys. Res.,* **93,** 8869–8891.

Lekic, V., French, S.W. & Fischer, K.M., 2011. Lithospheric Thinning Beneath Rifted Regions of Southern California, *Science,* **334,** 784–787.

Lund, B. & Townend, J., 2007. Calculating horizontal stress orientations with full or partial knowledge of the tectonic stress tensor, *Geophys. J. Int.,* **170**(3), 1328–1335.

Meade, B. & Hager, B., 2005. Block models of crustal motion in southern California constrained by GPS measurements, *J. geophys Res,* **110,** B03403, doi:10.1029/2004JB003209.

Michael, A.J., 1984. Determination of stress from slip data: faults and folds, *J. geophys. Res.,* **89,** 11 517–11 526.

Michael, A.J., 1987. Stress rotation during the Coalinga aftershock sequence, *J. geophys. Res.,* **92,** 7963–7979.

Montone, P., Mariucci, M.T. & Pierdominici, S., 2012. The Italian present-day stress map, *Geophys. J. Int.,* **189,** 705–716.

Mount, V.S. & Suppe, J., 1992. Present-day stress orientations adjacent to active strike-slip faults: California and Sumatra, *J. geophys. Res.,* **97,** 11 995–12 013.

Nicholson, C., Seeber, L., Williams, P. & Sykes, L.R., 1986. Seismic evidence for conjugate slip and block rotation within the San Andreas fault system, southern California, *Tectonics,* **5,** 629–648.

Nur, A., Ron, H. & Scotti, O., 1986. Fault mechanics and the kinematics of block rotations, *Geology,* **14,** 746–749.

Nur, A., Ron, H. & Beroza, G.C., 1993. The nature of the Landers-Mojave earthquake line, *Science,* **261,** 201–203.

Polet, J. & Kanamori, H., 2002. Anisotropy beneath California: shear wave splitting measurements using a dense broadband array, *Geophys. J. Int.,* **149,** 313–327.

Ron, H., Freund, R., Garfunkel, Z. & Nur, A., 1984. Block rotation by strike-slip faulting: structural and paleomagnetic evidence, *J. geophys. Res.,* **89,** 6256–6270.

Sauber, J., Thatcher, W., Solomon, S.C. & Lisowski, M., 1994. Geodetic slip rate for the eastern California shear zone and the recurrence time of Mojave Desert earthquakes, *Nature,* **367,** 264–266.

Savage, M., 1999. Seismic anisotropy and mantle deformation: what have we learned from shear wave splitting, *Rev. Geophys.,* **37,** 65–106.

Schmandt, B. & Humphreys, E., 2010. Seismic heterogeneity and small-scale convection in the southern California upper mantle, *Geochem. Geophys. Geosyst.,* **11**(5), Q05004, doi:10.1029/2010GC003042.

Scott, D.R., 1996. Seismicity and stress rotation in a granular model of the brittle crust, *Nature,* **381,** 592–595.

Shen, Z.K., King, R.W., Agnew, D.C., Wang, M., Herring, T.A., Dong, D. & Fang, P., 2011. A unified analysis of crustal motion in Southern California, 1970–2004: the SCEC crustal motion map, *J. geophys. Res.,* **116**(B11), doi:10.1029/2011JB008549.

Silver, P., 1996. Seismic anisotropy beneath the continents: probing the depths of geology, *Ann. Rev. Earth planet. Sci.,* **24,** 385–432.

Silver, P.G. & Holt, W.E., 2002. The Mantle flow field beneath Western North America, *Science,* **295,** 1054–1057.

Simpson, R., 1997. Quantifying Anderson's fault types, *J. geophys. Res.,* **102,** 17 909–17 919.

Shaw, J.H. & Shearer, P.M., 1999. An elusive blind-thrust fault beneath metropolitan Los Angeles, *Science,* **283,** 1516–1518.

Thatcher, W., Foulger, G.R., Julian, B.R., Svarc, J., Quilty, E. & Bawden, G.W., 1999. Present-day deformation across the basin and range province, Western United States, *Science,* **283,** 1714–1718.

Townend, J. & Zoback, M., 2004. Regional tectonic stress near the San Andreas fault in central and southern California, *Geophys. Res. Lett.,* **31,** L15S11, doi:10.1029/2003GL018918.

Townend, J. & Zoback, M.D., 2006. Stress, strain, and mountain building in central Japan, *J. geophys. Res.,* **111,** B03411.

Unruh, J.R., Hauksson, E., Monastero, F.C., Twiss, R.J. & Lewis, J.C., 2002. Seismotectonics of the Coso Range-Indian Wells Valley region, California; transtensional deformation along the southeastern margin of the Sierran Microplate, in *Geologic Evolution of the Mojave Desert and Southwestern Basin and Range,* Vol. 195, pp. 277–294, eds Glazner, A.F., Walker, J.D. & Bartley, J.M., Geological Society of America Memoir.

Wallace, R.E., 1951. Geometry of shearing stress and relation to faulting, *J. Geol.,* **59,** 118–130.

Walls, C., Rockwell, T., Mueller, K., Bock, Y., Williams, S., Pfanner, J., Dolan, J. & Fang, P., 1998. Escape tectonics in the Los Angeles metropolitan region and implications for seismic risk, *Nature,* **394,** 356–360.

Wang, C.-Y., Flesch, L.M., Silver, P.G., Chang, L.-J. & Chan, W.W., 2008. Evidence for mechanically coupled lithosphere in central Asia and resulting implications, *Geology,* **36**(5), 363.

Wesnousky, S.G., 2005. The San Andreas and Walker Lane fault systems, western North America: transpression, transtension, cumulative slip and the structural evolution of a major transform plate boundary, *J. Struct. Geol.,* **27,** 1505–1512.

Wüstefeld, A., Bokelmann, G., Barruol, G. & Montagner, J.-P., 2009. Identifying global seismic anisotropy patterns by correlating shear-wave splitting and surface-wave data, *Phys. Earth planet. Inter.,* **176,** 198–212.

Yang, W. & Hauksson, E., 2011. Evidence for Vertical Partitioning of Strike-Slip and Compressional Tectonics from Seismicity, Focal Mechanisms, and Stress Drops in the East Los Angeles Basin Area, California, *Bull. seism. Soc. Am.,* **101,** 964–974.

Yang, W., Hauksson, E. & Shearer, P.M., 2012. Computing a large refined catalog of focal mechanisms for Southern California (1981–2010): temporal stability of the style of faulting, *Bull. seism. Soc. Am.,* **102,** 1179–1194.

Zoback, M.D. & Healy, J.H., 1992. In situ stress measurements to 3.5 km depth in the Cajon Pass scientific research borehole: implications for the mechanics of crustal faulting, *J. geophys. Res.,* **97,** 5039–5057.

Zoback, M.D., Moos, D., Mastin, L. & Anderson, R.N., 1985. Well bore breakouts and in situ stress, *J. geophys. Res.,* **90,** 5523–5530.

Zoback, M.L., 1992. First-and second-order patterns of stress in the lithosphere: the world stress map project, *J. geophys. Res.,* **97,** 11 703–11 728.